3D electron microscopy investigations of human dentin and ion beam irradiation effect on biocompatible anatase TiO_2 using Focused Ion Beam based techniques

by

Sina Sadighikia

Submitted to the Graduate School of Engineering and Natural Sciences

in partial fulfillment of

the requirements for the degree of

Master of Science

Sabancı University

December 2015

3D electron microscopy investigations of human dentin and ion beam irradiation effect on biocompatible anatase TiO_2 using Focused Ion Beam based techniques

APPROVED BY:

Prof. Dr. Mehmet Ali Gülgün .....
(Thesis Supervisor)

Assoc. Prof. Dr. Melih Papila .....

Prof. Dr. Sedat Alkoy .....

DATE OF APPROVAL: 29/12/2015

3D electron microscopy investigations of human dentin and ion beam irradiation effect on biocompatible anatase TiO_2 using Focused Ion Beam based techniques

Sina Sadighikia

Materials Science and Nano-Engineering, MSc Thesis, 2015

Supervisor: Prof. Mehmet Ali Gülgün

Co-Advisor: Dr. Meltem Sezen

Keywords: FIB/SEM, 3D Electron Microscopy, Electron Tomography, Ion Beam Irradiation, Human Dentin, anatase TiO_2

Abstract

The essence of this study, in addition to the three dimensional image reconstruction of human dentin microstructure in micro and nano size; involves irradiation effects and modification of anatase TiO_2 surface by gallium focused ion beam, the various properties of modified surface were investigated by means of Scanning Electron Microscopy (SEM), Raman spectroscopy and Energy Dispersive Spectroscopy (EDS). The aforementioned procedures can successfully be carried out using a dual-beam system consisting of high-resolution scanning electron microscope (HR-SEM), focused ion beam (FIB) columns, attachments such as gas injection systems (GIS), and detectors for elemental analysis (EDS). However, the ion beam irradiation causes some artifacts along with other beneficial modifications on material's surface especially on biocompatible materials such as TiO_2. Therefore, in this study we considered the limitations as well as the advantages of using focused ion beam for nanostructuring, ion implantation etc.

In the first part of this study, high-resolution electron microscopy techniques, such as Focused Ion Beam (FIB), Scanning Electron Microscopy (SEM) and High Resolution Transmission Electron Microscopy (HRTEM) revealed micro and nano features within human dentin with high definition and accuracy. The samples were prepared using FIB based advanced nanostructuring processes in a dual-beam instrument. The related secondary electron (SE) image tomographs were acquired by means of stacking the images from FIB slice-series for monitoring micro-sized dentinal tubules, whereas FIB-structured pin-like samples were investigated at the TEM to observe the collagen fibrils at the nanoscale. The complementary analysis helped to reveal the microstructure and morphology of human dentin in three dimensions in detail.

In the second part of the study, surface morphology and microstructural evolution upon low energy ion irradiation of anatase TiO_2 were investigated by in situ focused Ga^+ ion beam/scanning electron microscopy. A surface roughening through pore formation, coalescence and eventually nanoneedle formation were induced on TiO_2 surface. The mechanism of nanoneedle formation was investigated. In addition, Raman spectroscopy and EDS analysis of irradiated surface revealed the gallium implantation during direct milling. Gas assisted etching was investigated in this study in order to reveal the enhancement of surface milling in presence of assisting gas.

3D electron microscopy investigations of human dentin and ion beam irradiation effect on biocompatible anatase TiO_2 using Focused Ion Beam based techniques

Sina Sadighikia

Malzeme bilimi ve nano-mühendisliği, MSc Tezi, 2015

Danışman: Prof. Mehmet Ali Gülgün

Ortak Tez Danışmanı: Dr. Meltem Sezen

Anahtar kelimeler: FIB/SEM, üç boyutlu Elrktron Mikroskopi, Elektron Tomografi, İyon Demeti Işınlama, Insan Dentini, Anataz TiO_2

Özet

Bu çalışmanın kavramı, dentinin üç boyutlu yeniden yapılandırma mikro ve nano boyutta, hem de ayrıca galyum odaklı iyon ışını tarafından ışınlama etkilerini anataz TiO2 yüzeyinde ve modifikasyonu içerir. Bu aşamada Taramalı Elektron Mikroskobu (SEM), Raman spektroskopisi ve Enerji Dağılım Spektroskopisi (EDS) vasıtasıyla modifiye yüzeyin farklı yönlerini araştırıldı. Yukarıda bahsedilen girişimlerin bir çift ışınlı sistemi kullanılarak gerçekleştirilebilir. Şu cihaz yüksek çözünürlüklü taramalı elektron mikroskobu (HR-SEM), odaklanmış iyon demeti (FIB), element analizi detektörü (EDS) ve gaz enjeksiyon sistemiyle (GIS) oluşmuş. Ancak, iyon demeti ışınlama faydalı değişiklikler sürece bazı eserlere malzemenin yüzeyinde neden oluyor Özellikle biyo-uyumlu TiO2 olarak malzemeler üzerinde. Bu nedenle, bu çalışmada, avantajlar yanında bu tür sınırlamalar göz önünde alındı.

Bu çalışmanın ilk bölümünde, yüksek çözünürlüklü elektron mikroskopi teknikleri (Odaklı İyon Işın (FIB), Taramalı Elektron Mikroskobu (SEM) ve Yüksek Çözünürlüklü Transmisyon Elektron Mikroskobu (HRTEM)), yüksek çözünürlüklü ve doğruluk ile

insan dentinin içindeki mikro ve nano özellikleri ortaya çıkardı. Numuneler, bir çift ışınlı cihazda FIB tabanlı gelişmiş nanostructuring işlemleri kullanılarak hazırlanmıştır. Ilgili ikincil elektron (SE) görüntü tomografları FIB dilim serisi görüntüleri istifleme suretiyle mikro-boyutlu dentin tübüllerini izlenmesi için elde edildi. Halbuki FIB yapılandırılmış pin-benzeri örnekler nano kollajen fibriller gözlemlemek için TEM de incelenmiştir. Tamamlayıcı analiz mikroyapı ve detaylı olarak üç boyutlu insan dentinin morfolojisini ortaya çıkarmak için yardımcı olur.

Çalışmanın ikinci bölümünde, yüzey morfolojisi ve mikrostructure evrimi düşük enerji iyon ışınlama anataz TiO2 üzerinede FIB ile incelenmiştir. Gözenek oluşumu yoluyla pürüzlendirme bir yüzey birleşme ve sonunda nanoneedle oluşumu, TiO2 yüzeyi üzerinde uyarılmıştır. Nanoneedle oluşum mekanizması incelenmiştir. Ek olarak, Doğrudan öğütme sırasında galyum implantasyonu, Oksijen boşluk oluşumunu ve amorfizasion Raman ve EDS analizleriyle ortaya çıkdı. Gaz destekli gravür Bu çalışmada araştırıldı.

Acknowledgment

Firstly, I would like to express my sincere gratitude to all who have never hesitated to support me by any means possible to fulfill this goal.

I would like to gracefully thank my advisor Prof. Mehmet Ali Gülgün.

Besides my advisor, I would like to express my special appreciation and thanks to my Co-advisor Dr. Meltem Sezen.

I would also like to thank my committee members, professor Melih Papila, professor Sedat Alkoy, for serving as my committee members.

I also would like to express my deep gratitude to all my friends who supported me in writing, and incented me to strive towards my goal.

Finally yet importantly, I wanted to salute the support of my lovely family who has always supported me by any means necessary.

Sina Sadighikia

To all genius people who found some meaning in the suffering

Table of Contents

List of Figures

List of Tables

Motivation

The use of Titanium Dioxide in biocompatible materials is becoming increasingly attractive for biological applications. Among various phases of TiO_2, Anatase and Rutile are the most extensively studied, due to their stability and vast variety of applications in energy storage and electrical materials. In addition, anatase is one the most significant materials in photocatalytic materials. In case of biotechnology, human dentin is one the most interesting materials in human body, which has gained a great, interest in materials characterization studies. Using TiO_2 based alloys in human tooth, as a biocompatible implant needs an understanding of human tooth and especially human dentin structure.

On the other hand, electron microscopy can be considered as a comprehensive and feasible technique concerning the microstructural and chemical analysis, as well as the modification of such biomaterials. Transmission electron microscopy enables a detailed investigation of the structures of these materials on a nanometer scale. Dual beam instruments, consisting of a scanning electron microscope (SEM) and a focused ion beam (FIB) column, additionally equipped with gas injection system and micromanipulators serve as multi- functional tools both for device modification and specimen preparation for TEM.

The irradiation of TiO_2 with ions can lead to temporary or permanent changes of its structure. The modification of the surface morphology of materials with ion beam irradiation has gained interest in materials science field. Obtaining a surface morphology with high specific surface area is always desired in various materials science fields such as biotechnology and energy storage materials.

The first part of the experimental study includes the three dimensional imaging and investigation of human dentin in order to reveal the interior microstructure of this material. For this reason the 3D image reconstruction technique of Focused Ion Beam (FIB) was used to explore the micron sized features inside the human dentin and furthermore the electron tomography studies has been carried on these features known as tubles in order to have a three dimensional structure view in nanoscale.

Another part of the study was focused on the analysis of the ion beam irradiation of TiO_2 during etching of the surface of this material by FIB. Raman spectroscopy technique was used in order to reveal the ion beam irradiation effects on TiO_2 surface including

amorphization, oxygen vacancy production and gallium implantation. A study of surface morphology evolution during ion beam irradiation has been carried out on TiO_2 surface in anatase phase. An interesting nanostructure known as nano-needle was obtained during ion beam irradiation. This nano-needle structure could play a significant role in biocompatible materials such as implantation for human tooth due to its high specific surface area.

1. Introduction

1.1. Scanning Electron Microscopy (SEM)

The scanning electron microscope (SEM) and its various detectors are one of the most multifaceted instruments with different applications from the investigation of the morphology of surface microstructure to chemical composition characterizations[1]. Among different types of electron microscopes that produce images due to electron sample interaction gained information, the SEM is an instrument for imaging the sample surface by scanning it with high-energy electron beam. The advantage of SEM over transmission electron microscopy (TEM) is the ability of SEM to image and analyze bulk specimens[2]. Since the electrons hitting the sample obtain high range of energies, in the case of thin specimen, they may have enough energy to transmit through it unabsorbed. These electrons can produce valuable information about the specimen, which is used to produce images in TEM. In case of a thicker specimen, electrons are no longer able to transit through the specimen and the information confines to different particles (e.g. electrons, x-rays and photones) rising from the surface. These signals are used in a typical SEM. The information which can be collected from an SEM can be categorized in the range of surface topography, crystalline structure, chemical composition and electrical behavior of the top 1 μm of the specimen.

1.1.1. SEM electron optics

A typical SEM column is shown in Figure 1. Within this column, due to the voltage difference between cathode and anode (ranging between 0.1-50 keV) electrons from a thermionic, Schottky or field emission cathode are accelerated.

By demagnifying the smallest virtual cross-section of the electron beam near the cathode with electron optics, a SEM produces a small electron probe at the specimen. In SEM system parameters such as electron prob size, aperture and the current are directly dependent on the gun brightness. To date several types of electron guns have been developed:

- *Tungsten hairpin filaments* are the most common ones. It acts by producing thermal emission of electrons from its tip. For this aim, the filament is thermally excited (via applying high electrical currents) to around 2500℃.

- The *lanthanum hexaboride (LaB_6) filament* is also a thermal filament and works by thermionic emission. However, its work function is lower than for a tungsten filament, so it is more efficient. Advantages comprise of a bigger maximum beam current, a brighter beam and a longer life time. However they are more expensive.

- *Field emission guns (cold cathode emitters)* due to the very high electric field and quantum mechanical tunneling of electrons on finely pointed tip a beam with high brightness with very small deviation in electron energy can be obtained. While thermionic guns require a vacuum of about 10^{-6} Torr, FEGs require lower than 10^{-10} Torr pressures to protect the tip which adds extra costs (for vacuum systems) for using these types of guns.

- *Schottky emitters* are known for their high brightness (10^8 A/cm^2) and high current stability. A Schottky emission cathode consists of a ZrO coated tungsten wire with a tip radius of 0.1-1 μm. The work function is dropped from 4.5 eV to 2.7 eV by applying a ZrO coating. The low work function enables the electrons to emit at a temperature of 1800 K.

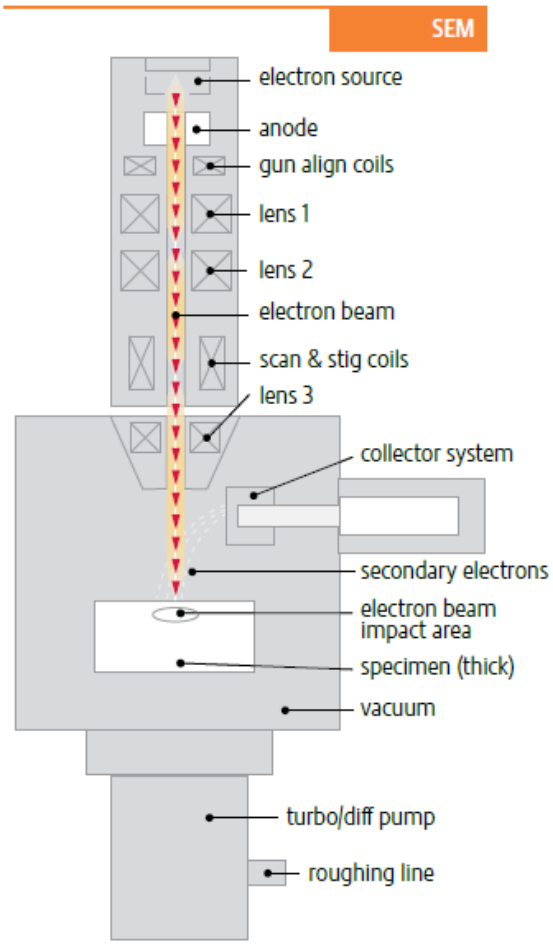

Figure 1 Basic SEM column

For demagnifying the electron beam into a fine probe in an SEM column, 2 to 3 electromagnetic condenser lenses are embedded. Via scan coils the electron beam is scanned across a particular zone of the sample surface. An electron lens comprises of an axial magnetic field with rotational symmetry. However, there are some limitations related to lens aberrations, which affect the quality of electron-probe and have to be considered. There are three types of aberration, which are important in scanning electron microscopy:

- *Spherical aberration*, which occurs when electrons which are parallel to the optic axes but at different distances from the optic axes fail to converge to the same point.
- *Chromatic aberration* is a consequence of a lens having a different refractive index for different wavelengths of lighting. This results in focusing of different wavelengths at different points.

- *Astigmatism* is another important type of lens defect, which happens due to magnetic inhomogenities of the pole pieces. If an optical system whit astigmatism is used to form an image of a sphere, the vertical and horizontal lines will be in sharp focus at two different distances, which may end up with an elliptical shape.

The electron spot size determines the spatial resolution of the SEM. This electron spot size depends on several parameters. Among these parameters, the wavelength of the electrons and the electron-optical system, which produces the scanning beam, play a significant role. Another important parameter, which restricts the resolution, is the dimensions of the interaction volume [3].

1.1.2. Signals and Imaging in SEM

The interaction of electron beam whit a bulk sample causes repeated scattering and absorption of electrons due to lose of energy. These phenomena occur within a teardrop-shaped volume of the sample (100 nm to 5 μm) up to the surface and known as the interaction volume. The electron beam energy is the determining parameter of the interaction size; however, other parameters such as the atomic number of the specimen and the specimen's density are also affecting it. The main information about the surface topography comes from the inelastically scattered electrons, which are produced due to energy exchange between the electron beam and the sample. These electrons are known as secondary electrons. The reason for emission of electromagnetic radiation and elastically scattered electrons is the energy exchange between the electron beam and the sample. In order to image the sample various signals from the specimen can be gathered (Fig. 2) as follows:

- *Secondary Electron (SE) images:* The electrons, which escape from the specimen with lower energies (usually lower than 50 eV), are known as secondary electrons. These electrons chiefly thumped out of their orbits around an atom (usually from the k-shell) by an incident electron. Since these electrons escape from an exceptionally shallow, close surface layer of sample, provide the highest spatial resolution images, which contain information about the morphology and topography of material's surface. However, since a few back-scattered electrons also collected by secondary

electron detector, some compositional contrast is also present. The contrast is dominated by the so-called edge effect: more secondary electron can leave the sample at edges leading to increased brightness there (Fig. 3)

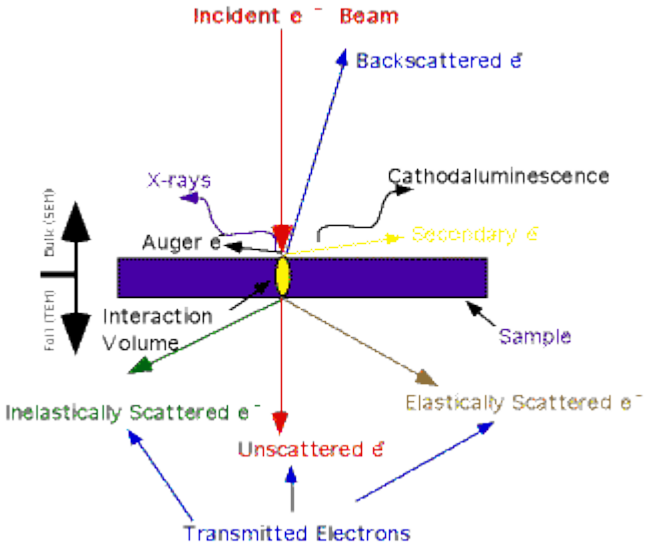

Figure 2 Signal generation due to specimen-electron beam interaction

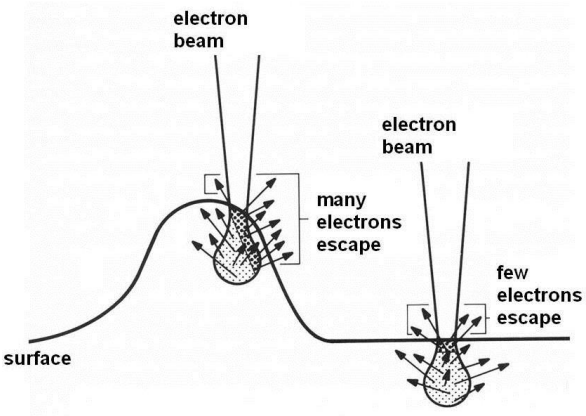

Figure 3 Edge effect in imaging with secondary electrons

- *Backscattered Electron (BSE) images:* Those electrons, which have enough energy to approach the nucleus of an atom adequately nearly usually, scatter through a large angle and energies. These electrons are known as backscattered electrons (BSE). Since they come from a region a little bit deeper than where secondary electrons come, the images produced by backscatter electrons have slightly less resolution. For the most part, they give compositional data: elements of higher atomic mass give brighter contrast. Backscattered electrons can likewise give crystallographic data, as electron channeling occurs.

- *Electron Beam Induced Current (EBIC):* in semiconducting specimens, incident electrons may generate several electron-hole pairs. Ordinarily, most recombine within about 10^{-12} seconds. Be that as it may, if an electric field splits the electrons and holes before they can recombine, an impelled current flow between the electrodes will occur, leading to the formation of an EBIC image.

- *Cathodoluminescence (CL):* Light emitting is one of the probable consequences when electron-hole pairs produced by the incident electron beam recombine. The wavelength relies on upon the band gap energy of the sample and in this manner on the composition. Prior to measuring by an appropriate identifier, the signal may pass a spectrometer. This strategy is magnificent for uncovering defects that debase radiative characteristics. Catodoluminescence signals originate from the entire specimen-beam interaction volume, so have a resolution of about 1 nm.

- *Voltage-contrast imaging:* There is difference between secondary image of a semiconductor produced with applied voltage and one with no voltage; the potential created over the dynamic regions changes the quantity of secondary (low energy) electrons released from those areas. Extra electrons can eject from active zones where a negative voltage is produced, so these appear brighter regions where a positive voltage is created.

- *Auger electrons and x-rays:* After an internal shell excitation, an atom possesses an energy higher than its relaxed state. There are two main ways out of several ways that the atom can relax and release some of this energy. Both begin with an outer electron jumping in to fill the vacancy in the inner shell. Characteristic X-ray emission: Energy is radiated as a single X-ray photon. Auger electron emission: Energy is given off by one of the outer electrons leaving. It conveys a characteristic kinetic energy. Auger electrons are emitted from atomic layers very close to the surface and give significant information about the surface chemistry. Measurement of the energies (or wavelengths) of these x-rays gives information about the chemical composition of the specimen. Characteristic x-rays are emitted from the entire specimen-beam interaction volume (Fig. 4). There are two different ways to detect the x-rays: energy dispersive or a wavelength-dispersive spectrometer. One of the most common attachment to SEMs for qualitative analysis of the specimen is Energy dispersive x-ray spectroscopy (EDS or EDX). This information can be used for 3D quantitative analysis of specimens as well.

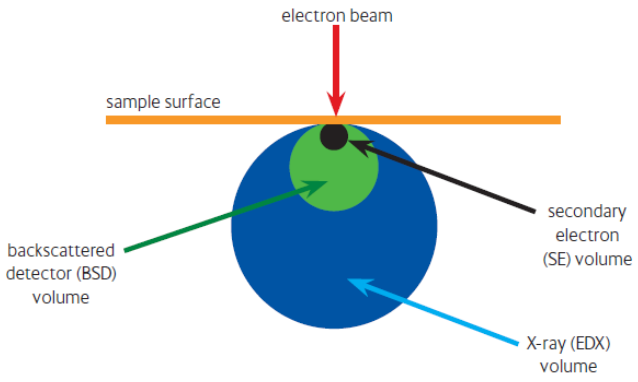

Figure 4 The interaction volume of electron beam and the specimen

The Everhart-Thornley detector is the most effective detector for secondary electrons (SE) (Fig. 5). Electrons are collected by a positively biased grid in front of a scintillator biased at +10 kV. The light emission is recorded by a photomultiplier tube.

If the solid angle of collection is increased, the scintillation detectors can also be used for backscattered electrons (BSE). Other choices for BSE are semiconductor detectors, microchannel plates or the switch of BSE to SE.

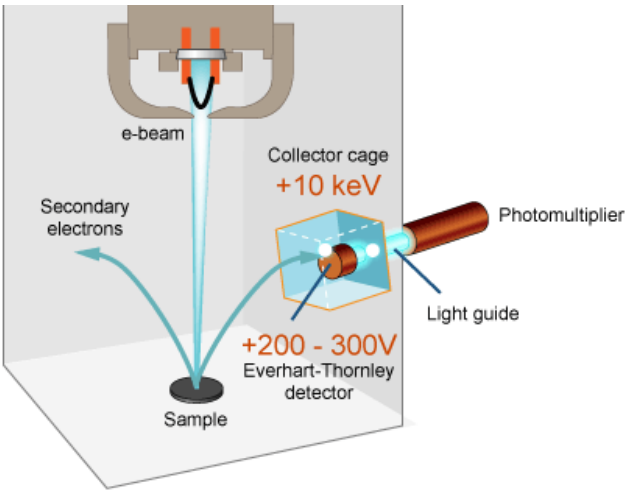

Figure 5 A typical Everhart-Thornley detector

For producing images, there are some electronic devices, which are used to reveal and magnify the signals. For displaying them as an image, it uses a cathode ray tube in which the raster scanning is synchronized with that of the microscope. The image is a result of a distribution map of the intensity of the signal being emitted, which is acquired from the scanned area of the specimen. The image can be captured either by photography from a high-resolution cathode ray tube or digitally on a computer monitor.

In an SEM, the ratio of the dimensions of the raster on the specimen and the raster on the display device defines the magnification. Assuming that the display screen has a fixed size, higher magnification results from reducing the size of the raster on the specimen, and vice versa. Magnification is therefore controlled by the current supplied to the x-y scanning coils, and not by objective lens power[2].

1.2. Focused Ion Beam (FIB) Microscopy

Focused Ion Beams (FIB) is one of the outstanding technologies as far as site-specific analysis, imaging, milling, deposition, micromachining, and transmission electron microscopy (TEM) sample preparation of materials are concerned. For more convenience, FIB instrument may be incorporated into other analytical instruments. The most versatile of those is a dual beam platform of FIB /SEM will be introduced in the next section.

There are some minor differences between FIB instrument and scanning electron microscope (SEM) and generally, they are similar to each other, except that the beam is rastered over the sample is an ion beam rather than an electron beam[4]. The main components of a simple single FIB instrument are vacuum system and a chamber, a liquid metal ion source, an ion column, a sample stage, detectors, gas supply and transfer system and a computer for running the whole apparatus.

As in most cases, implementation of ion beam for investigations necessitates the use of vacuum systems. For the simplest FIB instrument, having two vacuum pumping regions, one for the source and ion column and one for the sample and detectors are necessary. Nowadays, for more convenience a third system is also utilized for faster sample exchange. Like field emission SEM sources a FIB require a vacuum i.e., approximately $1x10^{8}$ torr to prevent contamination of the source and to avoid electrical discharges in the ion column while applying high voltages. Lower vacuum levels (i.e. $1x10^{6}$ torr range) are acceptable for the sample chamber however; higher pressures ($1x10^{4}$ torr range) will lead to the interaction of the ion beam with gas molecules. This is mainly due to the reduction of the mean free path at high pressures where the ions can no longer bisect the distance to the sample without undergoing collisions with the gas atoms or molecules. Considering these facts, due to their ability to provide higher vacuum levels, ion pumps are suitable choices for the ion source compartment while turbomolecular pumps backed with suitable rotary pumps are the typical choices for the sample and the exchange compartments [5].

In common FIBs, a liquid metal ion source (LMIS) is used for generation of the ion beam with a diameter of about 5 nm. Generally, a typical LMIS is a tungsten (W) needle which is connected to a metal source reservoir. Numerous pure and alloyed metallic sources are available for being used in LMIS. But due to some important advantageous which has been described in the few upcoming lines, gallium (Ga) has been preferred to other metal sources in commercial FIB instruments:

i. The low melting point of Gallium (T_m = 29.8 C) which minimize any counteraction or inter-diffusion of the liquid metal to the tungsten needle.
ii. Low evaporation rate of the Ga at its melting point, which yields to a durable source (can be used for longer time).

iii. Viscous behavior on the (usually W) substrate is boosted by the low surface free energy.

iv. Gallium has exceptional mechanical, electrical and vacuum properties.

v. High angular intensity with a small energy spread due to the emission characteristics of gallium.

In gallium LMIS, gallium metal located in such a way, that it has contact with a tungsten needle and heated. The emission of the Ga^+ occurs in two stages: Primarily, gallium wets the tungsten needle with a tip radius of about 2-5 μm, and an extensive electric field (greater than 10^8 volts per centimeter) causes ionization and field emission of the gallium atoms in the shape of a Taylor cone. Due to the electrostatic and surface tension force balance that is set by applying electric field, the aforementioned conical shape is formed. Then, once this force balance is achieved, because of the very fine tip of the cone, the extraction voltage pulls gallium from the tungsten tip, resulting in the ionization by field evaporation of the metal at the tip of the Taylor cone [6].

The current density of the ejected ions is around 10^8 A/cm^2.For creating the Taylor cone, which results in emission current, a finite voltage is needed. The source is generally operated at low emission currents (about 1-3 μA) to reduce the energy spread of the beam and to yield a stable beam. The intrinsic properties of the material and its quantity in the melt pool play a significant role in the lifetime of a LMIS, which can usually be stated in terms of μA-hours per mg of the melt (molten metal). An average lifetime for a source gallium is around 400 μA-hours/mg.

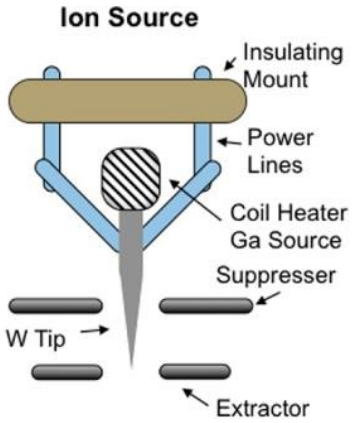

Figure 6 An illustrative representation of a LMIS

Once the Ga^+ ions are extracted from the LMIS, they are accelerated down to the ion column to an energy ranging from 5-50 keV and then focused onto the sample by electrostatic lenses. Figure 8 shows a schematic of the FIB column. The ion column normally consists of two lenses, a *condenser lens* and an *objective lens.* The earlier is the probe-forming lens and the later is employed for concentrating the beam of ions at the surface of the specimen. A wide range of beam currents is attainable (few pico ampers to 20-30 nA). Adjusting the beam shape can be accomplished by centering each aperture, tuning the column lenses, and fine-tuning the beam via utilization of the stigmators. Cylindrical octopole lenses are exploited to perform multiple functions such as beam deflection, alignment and stigmation adjustment. Additionaly, the scan field may be rotated by means of octopole lenses.

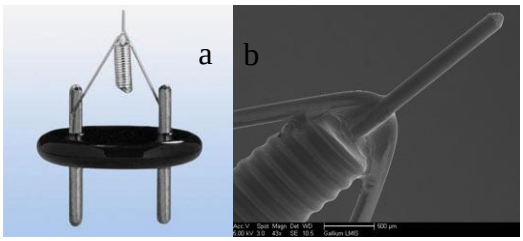

Figure 7 a) LMIS socket with filament; b) apex region of the filament with needle

The produced ion beam by an ion source is not really pure. Although the source produces the desired ion species, still due to contamination of the fuel there are other ions present, in addition there are some contributions of material by other parts in the source and fuel components. Moreover, the ions are subject to deflection by a magnetic field or an electric field, which are moving in a stream. For any particular magnetic or electric field, different ion species are directed along known but different paths. Furthermore, the selected ion species can be directed along a preselected path, even a straight line, when the correct orientation and field strength of both the electric and magnetic fields are employed. In such an ion analyzer, the electric and magnetic fields are at an angle to each other, usually at right angles to the ion path. Due to this orientation, they are commonly called E cross B filters, which is in jargon written as ExB[7].

The focusing of the beam is carried out via magnetic lenses in both SEM and TEM. The Lorenz force is much lower for the ions because they are much heavier and slower. Hence, magnetic lenses become less effective for the ions in comparison with electrons of the same energy. Therefor magnetic lenses have been replaced by electrostatic lenses in FIB

systems. Another reason for this is the fact that Ga^+ ions have two isotopes and in case of using electromagnetic lenses there will be two different confocal points.

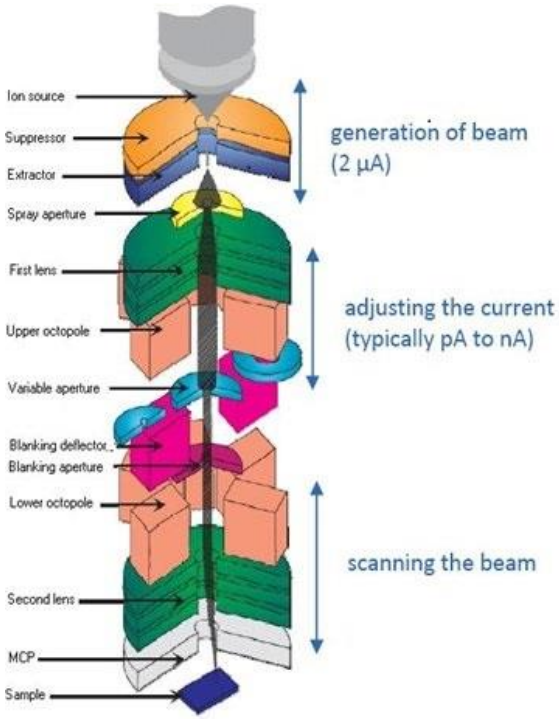

Figure 8 Cross section of a basic FIB column

Field variation is negligible for the samples with varied topography because FIB systems benefit from large working distance (~ 2 cm or less). The provocation of different species such as sputtered atoms and molecules, secondary electrons and secondary ions happens when gallium cations hit the sample. More information on this subject will be given in the subsequent parts of this thesis, where specimen-beam interaction is discussed.

Even a precisely confined ion beam suffers from larger energy spread in comparison with an electron beam (around 5 eV). Due to the massiveness of the ions compare to electrons, space charge effects restrain the seeming source size and widens the energy distribution of the producing ions. This means, the dominant restricting parameter in the resolution of a FIB instrument is its chromatic aberration. Other important aberrations in a lens system may be spherical aberration and astigmatism, which were already mentioned in the previous section for SEM.

In order to have an image in FIB two different kind of detectors which collect secondary electrons can be used, a multi-channel plate (MCP) or an electron multiplier (EM). A

MCP is typically attached straight overhead of the specimen. On the other hand, the EM is regularly aligned to one side of the ion column. Both secondary electrons and secondary positive ions which are ejected from the sample are detectable by means of the electron multiplier detector. It is noteworthy that even during imaging with FIB the sample is being sputtered; thus tiny beam currents (<100pA) are usually used for FIB imaging to lessen material loss during imaging.

Numerous contrast mechanisms are possible for providing diverse imaging abilities. Secondary electrons (SE) offer images with decent depth of field. Nevertheless, secondary ions (SI) result in diverse kind of contrast in comparison with the SE, because oxides and carbides have effect on the secondary ion yield of the metal, SI images are mainly sensitive to the existence of these elements in metallic systems. The more increasing in the brightness of a region containing metal oxides or carbides because of "enhanced yield" of oxygen or carbon, creates a chemical contrast effect that makes FIB SI imaging an ideal technique for identifying corrosion or grain boundary segregation without resorting to chemical etching.

Regarding our intention, various kinds of produced particles can be detected with proper detectors in the sample chamber. Numerous types of detectors are available for detecting the electrons or the x-rays coming out of the specimen after being hit by the ion beam, such as those in an SEM. The ejected ions, are also detectable by a variety of detectors such as charge electron multipliers and mass selection of the sputtered charged particles is also possible by secondary ion mass spectrometry (SIMS)[4].

1.3. Dual-Beam (SEM/FIB) Systems

A *dual-beam* (DB) or a *cross-beam* instrument incorporates both a FIB column and a SEM column in a solitary system. This arrangement has the advantage of viewing FIB functions by means of an SEM. It is especially useful for cross-section sample observation using the electron beam (SEM) while the ion beam mills normal to the sample surface, and it is beneficial to view the TEM sample preparation procedure by FIB. The common DB-column arrangement is a vertical electron column with a tilted ion column. Figure 9 displays this arrangement where the ion beam is tilted 52º vertically, providing the milling process normal to the sample surface. Different platforms may have different tilt angles for ion beam column varying from 52º to 55º.

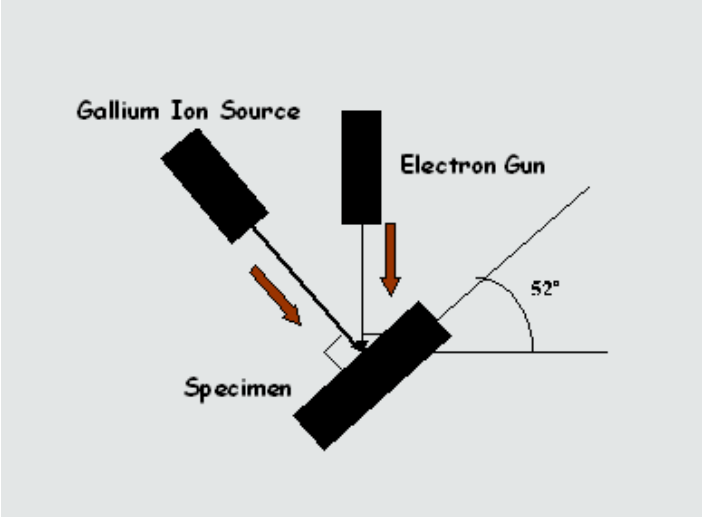

Figure 9 A DB system configuration

To enable the use of electron beam and ion beam on the matching area, dual beam instruments usually have a coincident focus point, *eucentric point*, where both beams cross from an identical point. Reaching this point requires setting the working distance to the eucentric height, which again varies for different platforms and can be a distance from 5 mm to 9 mm for the electron beam at 52˚to 55˚.

In addition to electron and ion columns, a commercial FIB may be equipped with other systems as shown in Figure 10, which provide additional *in-situ* processes within the microscope such as spectroscopy, deposition, etching and manipulation.

In order to have the capability of site-specific deposition of metals or insulators Gas injection systems (GIS) can be used in conjunction with the beams. This capability can enhance the etching process. Metals such as, platinum or tungsten may be deposited by electron or ion beam assisted CVD of a precursor gas containing these metals in their structures such as $C_7H_{17}Pt$ or $C_9H_{16}Pt$. Principally in a beam-induced deposition the precursor gas covers the surface of the target substrate and incidence of the beam leads to its decomposition, releasing the metal on the surface[8]. Finally, dissociated molecules are adsorbed and deposited to the defined patterns in dual-beam systems.

Dual-beam systems can also be used in acquiring chemical spectra and elemental maps by means of energy-dispersive spectroscopy (EDS). By combining controlled ion milling with chemical mapping, three-dimensional chemical reconstructions can be obtained[9].

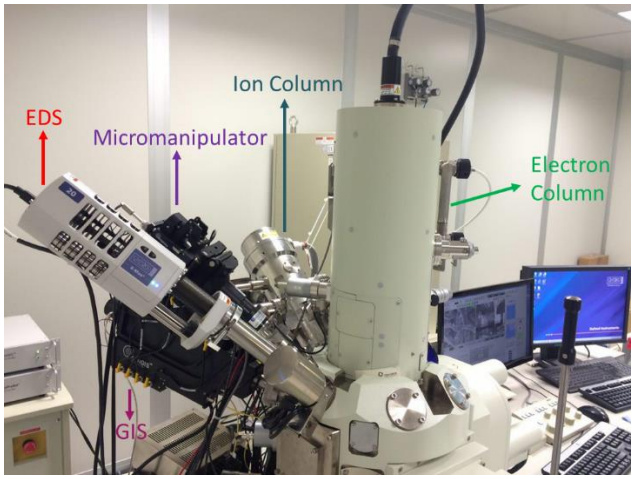

Figure 10 The dual-beam FIB system (Jeol JIB 4601F)

Using an integrated dual-beam system, many feasible issues can successfully be carried out concerning material science, nanotechnology, semiconductor technology and biosciences. Some of the frequently used dual-beam techniques will be presented in the following section.

1.3.1. Dual Beam Applications

1.3.1.1. TEM Specimen Preparation

Sample preparation for transmission electron microscope (TEM) investigation is one of the most significant applications of a dual-beam tool. For a reasonable penetration of a beam of electrons, TEM samples must be uniformly thin. with FIB we can produce, uniformly thick, site-specific samples. In case of composite materials comprised various organic and inorganic substances FIB provides a possibility to fabricate lamella.

The major benefits of utilizing an FIB for TEM sample preparation are:

- It is possible to select the target very precisely with FIB. It has the capability to prepare lamella with a spatial accuracy of within about 20 nm.
- Compare to other techniques TEM sample preparation with FIB is fast and reliable; it can be vary in the range of 20 minutes to a maximum of 2-4 hours, specimens can be prepared with almost no restriction in terms of material variety.
- TEM sample preparation with FIB based techniques is not dependent on the target substance. Due to optimization of the geometry and properties of the

protective layer on the sample surface it is virtually possible to perform the milling process on various materials [10].

The most straightforward method for TEM specimen preparation which is shown in Figure 11, is also called ‘‘in-situ lift-out technique’’[11]. The procedure is based on several steps starting with a deposition layer of a protecting gas such as platinum or carbon conducted either by ion or electron beam. Milling two opposing trenches with the Ga^+ ion source and leaving a 1-2 µm thin section is the next step. The procedure goes on with cutting the bottom and the side trenches away until the section is hold by the bulk sample from its shoulders. Then, the section can be welded to the micromanipulator by means of ion beam assisted platinum deposition (IBAD). The next step involves cutting away the shoulders, now the lamella is free and can be lifted out from the sample, transferred and attached to a TEM grid. Afterwards, final thinning and polishing in a thickness range of <100 nm is achieved using low incident angles and low ion currents. Finally, the sample is ready for TEM analysis.

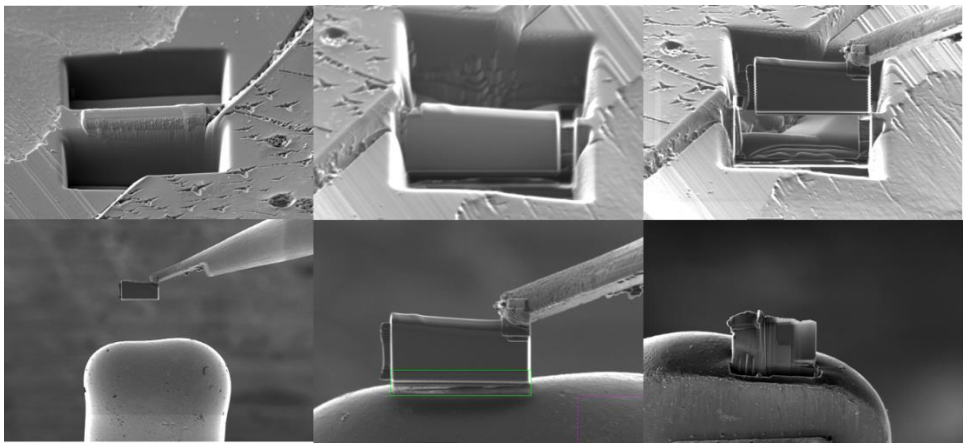

Figure 11 TEM specimen preparation of TiO2 rutile using a dual beam tool, coarse milling, lift out, mounting and thinning steps

In addition to this route, there are many more procedures in the literatures, which have been developed for more than a decade. Some of the most important and widely used methods includes, trench[12], H-bar, ex-situ lift out[10], plan-view and H-bar lift-out[13] and cantilever[14] techniques. However, in this study we developed a new method for TEM sample preparation with FIB, which is proper for electron tomography investigations. In the current work, FIB was successfully utilized for the TEM specimen preparation of human dentin. This will be discussed in subsequent chapters.

Although it is possible to prepare TEM samples from various kind of materials by FIB but this method is often applied for hard materials (e.g. metals, glass, ceramics) or layered structures (e.g. semiconductors) with hard substrates (silicon, glass, etc.). Soft materials are sensitive to ion milling due to beam damage and heat dependent shape distortion. For soft materials, ultramicrotomy[15] is considered to be the most convenient preparation technique, which is a mechanical sectioning process using a diamond knife.

1.3.1.2. Slice & View Method for 3D Imaging

The possibility of using the ion and electron beams simultaneously in most of the dual beam instruments opens a way to perform cross-sectioning by means of ion milling and to acquire electron beam images of the cross-section from the same region of the specimen. This method is called ‘‘slice and view’’ and often used for the investigation of multilayered or semiconductor samples. Compared to TEM specimen preparation this method is quite fast and convenient.

Collecting the data for three dimensional image reconstruction of volumes utilizing a dual platform FIB/SEM tool as a stack of 2D scanning electron microscopy (SEM) images can be performed in two different ways: in static or dynamic mode. In dynamic mode hence the name, SEM images are acquired in real time during the FIB milling process. In static image acquisition mode, after the FIB milling the ion beam either paused or stopped then the SEM image can be required which has high resolution due to slow scan[16].

With the application of slice and view process, it is possible to utilize dual beam systems for failure analysis in semiconductor devices. For instance, Volinsky et al. showed in their paper the identification several failure mechanisms in memory arrays, including milling patterns[17].

1.3.1.3. 3D Microstructural Characterization and FIB-Tomography

Dual beam instrument has the ability to provide three-dimensional information methodologies in order to have a reliable quantitative materials characterization. Specifically, with 3D imaging and characterization it is possible to measure a number of crucial geometric properties that cannot be attained utilizing a 2D analysis, such as the number of particles per unit volume, pore connectivity, real particle shapes and sizes and spatial dispersion information[18].

The basic principle for 3D tomography is collecting continuous 2D data from the surface of the bulk material by serial sectioning and combining them into a 3D volume by means of several computational processes (Fig. 12). Serial sectioning is applied by creating a planar surface by means of removal of the material volume by ion milling. For 3D image reconstruction, an area of interest is chosen and ion milling is used to create a trench around this area with high beam currents (5-20nA). The trenches must be adequately large in order to avoid redeposition of sputtered material and eliminate shadowing of imaging signals. A protective platinum film (about 1 μm thick) is deposited on the top surface of the volume of interest before trenching to avoid Ga^+ implantation. After these steps, serial-sectioning process can be initialized.

For complete removal of the total volume, the current and the milling time should be selected in a way to fulfill this fact. With the removal of each section, various signals could be collected depended on desired data. These data consist of SE images, BSE images, EBSD maps and/or EDS data which can be acquired from the specimen surface. All these data can be used for 3D reconstruction and 3D material characterization. Consequently, dual beam microscopes are capable of high-fidelity characterization of the morphology, crystallography and chemistry of micron- and submicron- sized features in 3D[18].

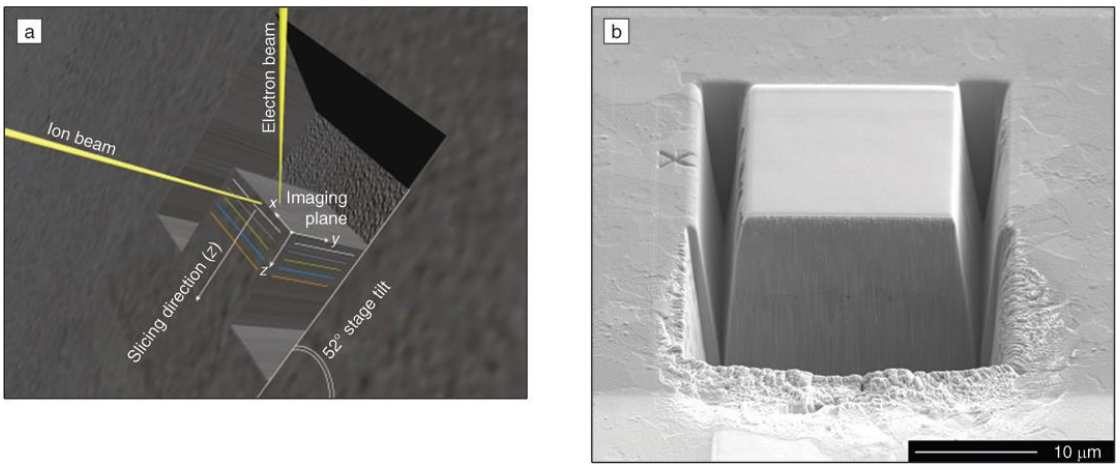

Figure 12 a) Schematic depict of a conventional sample for 3D image reconstruction b) SE image of a desirable sample for serial sectioning **(taken from[19])**

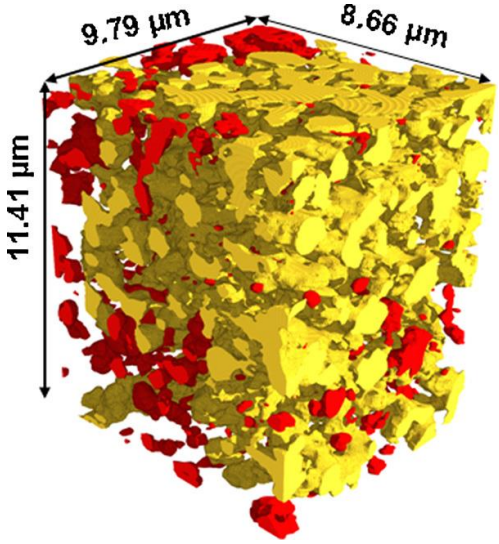

Figure 13 3D EDS image reconstruction which shows particle distribution in three dimensional volume **(taken from[20])**

There are even more applications for FIB/SEM dual beam platform such as micromachining, nanostructuring and mechanical testing. For instance recently some works have done for testing the influence of sample dimensions on mechanical properties known as "size-scale effects", particularly on metals and alloys[21], [22]. Besides the preparation of the test structure, FIB allows to conduct in-situ mechanical testing in micro/nano size when the system is equipped with mechanical-test-stage and nano-indentation devices. These mechanical properties include tensile strength[23], [24] and yield strength measurements[22] which is giving out the data in form of stress-strain curves.

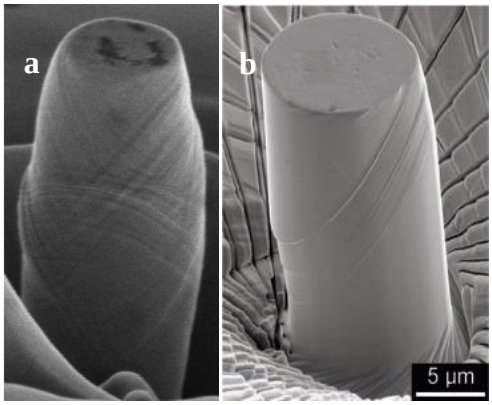

Figure 14 Examples of in-situ mechanical testing by FIB: a) comparision tests on a gold pillar (taken from[24]) b) yield strength/ plasticity test on nickel superalloy pillar **(taken from[22])**

1.4. Electron and ion beam irradiation on various materials

1.4.1. Electron beam irradiation

Affecting the organic or inorganic samples by electron beam when they are placed in electron microscope is unavoidable. The main effects can be electrostatic charging, ionization damage (radiolysis), displacement damage, sputtering, heating and hydrocarbon contamination. Two major parameters are important in electron beam damage: first, the amount of radiation damage, which is proportional to the electron dose and second the extent of damage, which is dependent on the amount of energy, deposited in the specimen[25].

Figure 2.1 shows the classification of electron beam induced sample damage according to scattering behavior. All of these effects will be discussed briefly in the subsequent paragraphs.

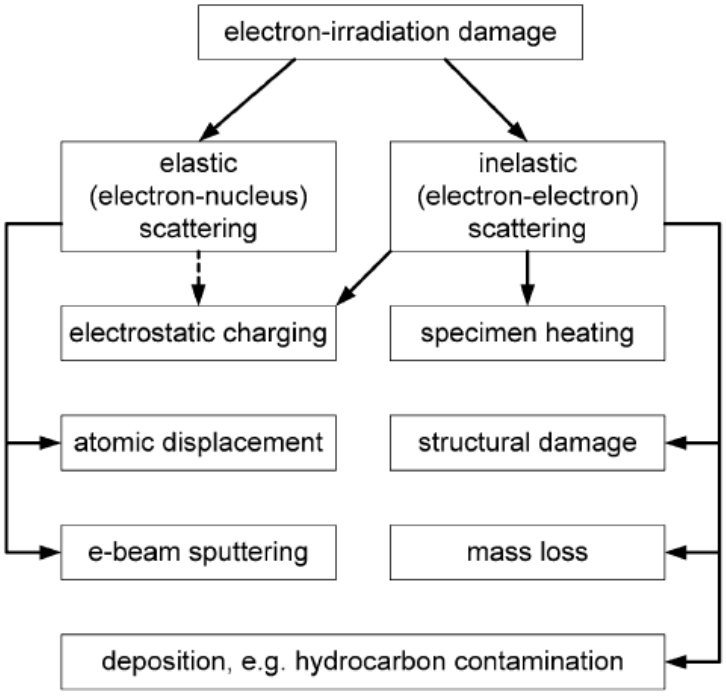

Figure 15 Irradiation damage classified according to electron scattering behavior **(taken from[25])**

The effect of the electron beam produced by both TEM and SEM may cause different temporary or permanent changes within the specimen. The scattering behavior of the

electrons plays a crucial role in the sort of damage. There are two distinct way of electron scattering when the electron beam hits the sample: elastic and inelastic scattering. Elastic scattering (also called as Rutherford scattering) represents the electrons, which are deflected in high angle by atomic nuclei of host atoms. In this case, the energy of deflected electrons is conserved and gives rise to electron diffraction patterns and backscattered electron images. However, it can also result in atomic displacement and sputtering of atoms within the structure. In the other hand, the inelastic scattered electrons are the electrons, which have interaction with the electrons of a host atom. In this case, the deflection angle is low and the initial energy of the incoming electrons has been changed. This kind of scattering results in production of secondary electrons, x-ray emission and electron energy loss spectra (EELS). The disadvantage is that all the inelastic processes the deposition of energy during inelastic interaction is almost unavoidable which can damage beam-sensitive specimens and leads to radiolysis, which causes structural changes and material loss[25].

1.4.1.1. Electrostatic charging

The accumulation of surface charge on or inside the specimen results in a phenomenon known as charging. Basically when the energy from the primary electrons is retained by the sample instead of being shed to an electrical ground, charging occurs. To avoid this issue, normally the poorly conducting specimens are coated by a conductive layer, which eliminates the image artifacts, which appear due to the exuberance surface charge during SEM analysis. The artifacts shows themselves as irregular, featureless bright patches, or streaks on SEM images and are generally follow by loss in resolution[26].

Electrostatic charging of low electrical conductive samples incorporates both elastic and inelastic scattering since the net charge added to the film per second depends both on the backscattering coefficient and on secondary electron yield[25].

Also in this study, it was necessary to coat the human dentin and Anatase (usually by sputtering) with conductive layers in order to avoid charging effects during SEM examinations. Even a few nanometers of metallic coatings were sufficient to see remarkable differences in SEM image quality.

1.4.1.2. Atomic displacement (Knock-on)

Although in elastic scattering the initial energy of the electrons is conserved, but there is still some amount of energy transferred to the nuclei of host atoms due to momentum transfer. The knock-on damage occurs when this energy exceeds the displacement energy. In this case the incident electron generates vacancies e.g. Frenkel defects due to knocking out an atom from its position by striking it. The energy required for the knock-on process varies with the atomic number of the sample. This is not a significant issue in SEM because the energy threshold for knocking out an atom is considerably high. For example, for carbon with atomic number of 6 the knock-on threshold energy is about 80 keV, and this energy for silicon (Z=14) the knock-on threshold is 220 keV[25].

1.4.1.3. Electron beam sputtering

When the atoms are knocked out of the specimen to the vacuum due to the interaction whit electron beam, we call it electron beam sputtering which is usually a high-angle elastic scattering process. This transferred energy in the electron beam sputtering is very similar to atomic displacement despite the fact that the transferred energy is much lower. Here the incident energy needed for sputtering should pass the sublimation energy of the atoms. According to the study from Egerton and Malac[25], the threshold energy for electron beam sputtering increases with the atomic number (Z), and therefore sputtering is most likely to happen for the elements with low atomic numbers.

To avoid this problem limiting the irradiation dose can be helpful. In another case where there is a need to use high doses, coating the sample with a heavy element as a protective layer can solve the problem.

1.4.1.4. Electron beam heating

As we mentioned above inelastic scattering takes place when the electron beam collide with the electrons of host atoms. The transferred energy may convert to heat during this process and cause a local temperature rise. However, thermal damage is not usually a serious problem for the materials with medium density and the thermal diffusivity as the energy deposited is quite small, and the ultimate temperature rise with energy and beam dose is minimal.

Due to incorporating of various variables, measuring specimen heating experimentally is difficult. The experimental variables that can affect the result include energy and current, thermal conductivity, surface condition, thickness and the beam size.

1.4.1.5. Radiolysis (Ionization damage)

Another effect of inelastic scattered electrons is the breakage of the molecules bonding due to ionization. This dissociation of molecules by radiation is known as radiolysis.

In radiolysis process, molecule changes in form and shifts in position and the chemical bonds are broken so the material loss the crystallinity and as a result swelling and shrinkage are the major problems in ionization damage, which may cause even material loss.

There are different ways to overcome this problem. The most cheap and convenient way is coating the specimen with a metal layer. Besides, since the radiolysis is a temperature dependent process, cooling the specimen down to cryogenic temperatures can be a solution during electron microscopy applications.

1.4.1.6. Hydrocarbon contamination

Incoming electrons may cause the polymerization of hydrocarbon molecules on the surface of a sample. In this case, mass gain occurs on the sample. The low vapor pressure and low surface mobility are the characteristics of this polymer layer which cause increase in thickness as the irradiation goes on[25]. It is nearly inevitable to have hydrocarbon molecules on the surface of specimen and these are typically formed in the vacuum of the microscope as a pressure of hydrocarbons or silicon oils from the diffusion pump[2]. Although the vacuum systems are alleged clean instruments, but they always have specific amount of hydrocarbon debris that the vacuum pumps do not adequately remove. The pump type plays a crucial role in cleanliness of the vacuum and the amount and nature of these debris molecules.

The diffusion of most hydrocarbons along the specimen can be the source of most contaminations. The shape of this diffusion is in a way that the hydrocarbons diffuse along the specimen's surface towards the edge of the irradiated area and immobilized.

There are many techniques for overcoming this problem and removing the contaminations. Heating the specimen with an electric lamp, which desorbs hydrocarbons from the surface, is one of these techniques. Exposing the specimen to the ions in plasma cleaner or inside the microscope is another solution. In addition using a cold finger inside the specimen chamber to reduce the mobility of hydrocarbons can be helpful. It is noteworthy that anything that reduces charging also reduces contamination, therefore

coating or pre-cleaning the samples prior to observation would help in minimizing hydrocarbon contamination[25].

1.4.2. Ion beam irradiation

There are various ways of interaction between an energetic ion, which enters a target, and the material. Based on the energy of ions, this interaction can be sputtering, amorphization, swelling, deposition, redeposition, implantation, backscattering or nuclear reaction. These interactions which are not divisible may point to undesirable side effect that need to be perceived and prevented for a particular application[27]. The high radiation damage is also induced since all of these events occur simultaneously. In this case, not only the morphology changes, but also we have changes in intrinsic physical properties (conductivity, electrostatic change, elasticity and crystallinity) and chemical characteristics (composition and hydrophilicity) of the surface[28].

Due to massiveness of ions compare to electrons, these particles cannot readily penetrate inside individual atoms of the sample and they can gain a high momentum. A 30 keV Ga^+ ion depending on the material can penetrate to a depth of 5-40 nm when it hits a surface. Since these ions have interaction with the atoms of materials they loss their energy and momentum. This causes the atoms to vibrate profoundly inside their lattice or even to break, which results in a collision cascade. It is possible to have many independent binary collisions within the material due to the collision cascade model. A critical amount of energy called displacement energy is needed to be transferred from the ions to the target atom in order to knock the atom out of its position. In this process, interstitial-vacancy pair in a crystalline sample will be introduced. Respectively the energy of this displaced atom may be sufficient to force out further sample atoms, this phenomenon generates a volume where a large number of atoms have exuberance kinetic energy. It is noteworthy that the displacement energy is much larger than the binding energy of the atoms (20 keV with respect to 1 keV for binding energy)[29].

Local temperature increase may cause amorphization and recrystallization in bulk materials however the melting temperature of material is related to the sputter yield. The sputter yield is a measure of the efficiency of the material removal, which defined as the number of atoms ejected per incident ion[27]. This factor is respectively high for a material with low melting temperature[30]. In addition to material removal, the ion

impact can cause a damaged layer on the specimen surface, which may extent several tens of nanometers into the material[9].

The transferred energy from the ions to the material may have divers impacts on sample such as specimen damage, specimen heating, electromagnetic radiation, electron emission, atomic sputtering and ion emission, ion reflection and backscattering as an outcome.

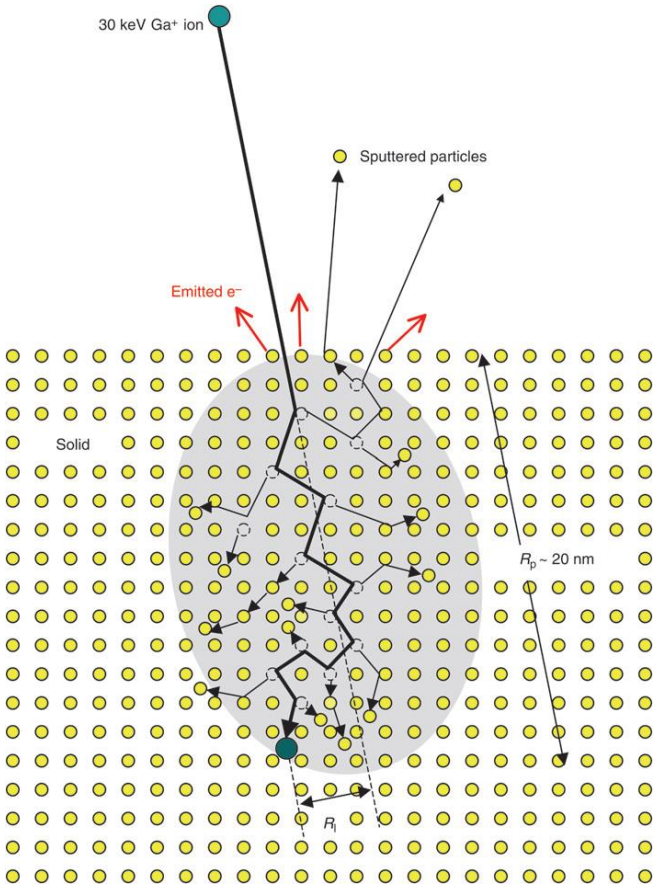

Figure 16 Schematic illustriation of collsion cascade generated in a crystal lattice by a Ga+ incident ion **(taken from[31])**

Implantation of the ion occurs when the incoming ion rests in the solid. All of these processes are important to dual-beam system application. Elastic and inelastic interactions are both incorporate in transferring the ion kinetic energy and momentum the specimen. Elastic interaction also called electronic energy loss is a kind of interaction in which the ions lost their energies to the electrons of host material, which results in ionization, and the emission of the electrons and electromagnetic radiation from the specimen. On contrary, in inelastic interaction the transferred energy is in the form of translational

energy, which screens the target atoms and can result in damage (displacement of atoms from their initial stage) and sputtering from the specimen surface[31].

In the subsequent sections, main mechanism for ion irradiation will be discussed.

1.4.2.1. Sputtering

The primary mechanism for material removal is known as sputtering. The efficiency for this material removal process is typically represented by sputter yield (Y), which can be described as the number of ejected atoms per incident ion. There are different parameters, which affect the sputter yield; generally, it raises with the ion energy. However, the incident angle plays a significant role in sputter yield. It is well known that the sputter yield increases by increasing the incident angle up to 80˚where the yield is maximized, and then it diclined very briskly to zero as the incident angle approaches to 90˚. Besides it is also dependent on target material. In general, the materials, which obtain low surface binding energies, can produce higher sputter yield as well as heavier ion sources.

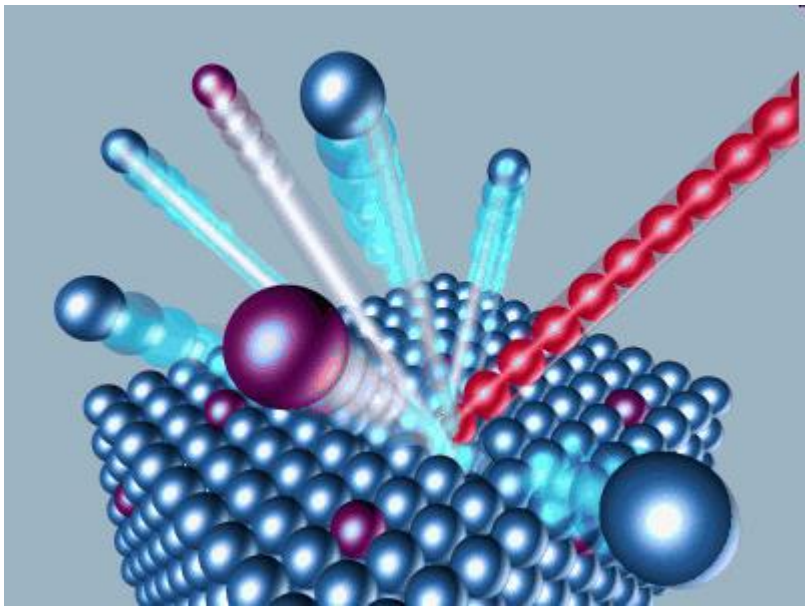

Figure 17 Schematic of etching material's surface with ion beam

1.4.2.2. Amorphization

Ion bombardment of a desired region on the specimen is the FIB procedure to selectively remove the material. In this way ion implantation can produce an amorphous phase surface. Amorphization occurs when the incident ion beam energy or dose is not enough to cause sputtering and remove the material. In this situation, the bombarded crystalline substrate may swell[27]. The amorphous phase formed in crystalline materials by ion

bombardment is normally meta-stable, and its production depends on unit cell size, intricacy of chemical ordering and the width of an intermetallic phase field[32].

The amorphization is a serious problem when FIB is used to prepare TEM samples. The amorphization of crystalline materials may lead to misinterpretation of the structures in TEM investigations. Because of this, there are extensive studies for overcoming this problem and minimizing the amorphous layer formation during FIB milling.

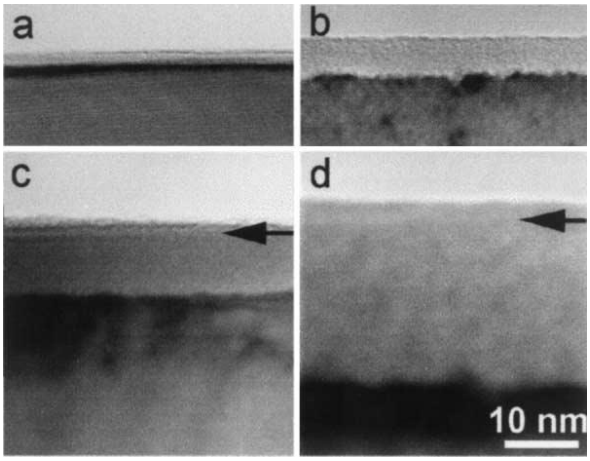

Figure 18 TEM images of the amorphized surface on different surfaces **(taken from[33])**

It is feasible to minimize this damage with using low energies of ions due to corresponding interaction volume. Cooper et al have shown that the amorphous layer formation reduces by decreasing the ion energy (Fig. 19)[34].

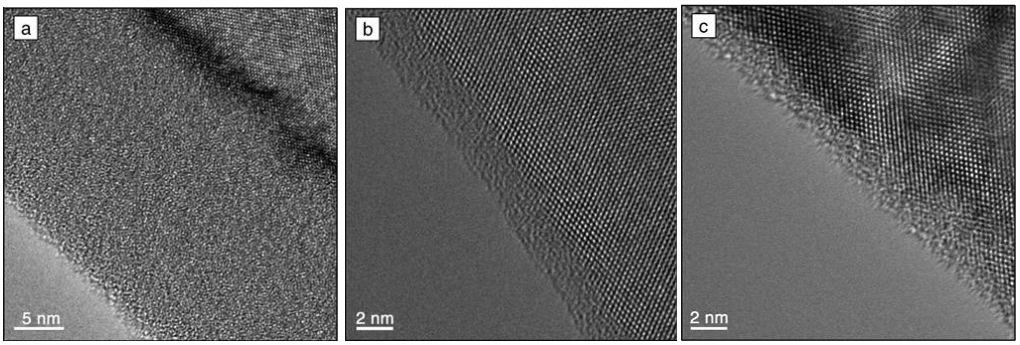

Figure 19 The comparison of formed amorphous layer in different ion energies. **(taken from[34])**

When low energies like 30 keV is used in FIB which is conventional Ga doping stays almost entirely inside the amorphous layer; however at even lower energies it is possible

that the gallium doped region extends beyond the amorphous depth. Therefore, it is noteworthy that polishing or low energy milling of TEM lamella will still cause Ga doping which can be a very rich layer as contamination even though imperceptible amorphous silicon remains on the surface[35].

1.4.2.3. Gallium implantation

The local composition may be influenced by gallium implantation since it can be mixed into the specimen because of the sputtering process. Kiener et al have found that the concentration of up to 20% gallium can be found several nanometers below the surface whereas gallium contents of more than 2% were observed inside a depth of up to 50 nm. They have measured these concentration depth profiles of implanted gallium by Auger electron spectroscopy[21].

Gallium implantation has various effects on the sample. It may affect thermal, electrical, optical, and mechanical properties as well as causing structural changes. Datesman et al revealed that as because of gallium implantation there is a decrease in transition temperature and partial increase in resistance of a 10 nm niobium film[36]. In addition it was shown by Kiener et al[21] that the mechanical properties could be affected by the gallium occupancy. Although gallium implantation is a destructive phenomenon but sometimes it can be intentionally used for structural and compositional modifications. For instance, gallium can be used as dopant implanted into a silicon substrate to locally modify the conductivity of silicon[37]. Also in this work a physical dope of gallium was induced on the surface of TiO_2 (Anatase) to modify the phase and band gap of the anatase.

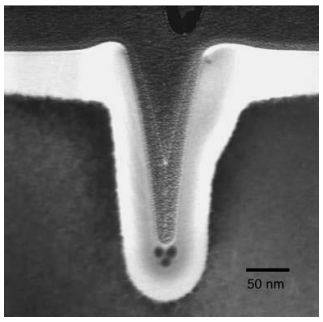

Figure 20 TEM image showing the implanted Ga^+ into the Silicon surface **(taken from[38])**

To prevent this problem in TEM specimen preparation usually a protective layer of platinum or other protective gas is deposited on the desired region however ion beam induced deposition (IBID) may implant gallium on the substrate. This may affect the

TEM interpretations due to irradiation dependent structural changes. In order to overcome this issue a protective layer of platinum is deposited on the substrate by means of electron beam known as electron beam induced deposition (EBID) prior to an ion beam induced deposition[39]. This EBID layer can be accepted as a non-destructive deposition method due to the weightlessness of electrons compared with ions.

1.4.2.4. Specimen Heating

Apart from a fraction of energy needed for defect generation and emission of energetic particles while ion implantation nearly all of the kinetic energy is ultimately transformed to heat. The ion beam can be as a constant heat source for times more than approximately a nanosecond and lengths longer than around 100 nm. Due to the shortness of time (less than 10^{-12} s), during heating which cause large temporal variations the atoms the interaction of atoms with each other is scarce and the temperature of the solid is not well determined. There are different parameters which determine the maximum temperature that a sample can reach. These parameters are: beam power *P*, sample thermal conductivity κ sample geometry and contact to a heat reservoir. In below equation a represents the radius of the circular ion profile on the surface.

$$T = P/(\pi a \kappa)$$

For materials with good thermal conductivity, this temperature rise is entirely negligible but for samples with poor thermal conductivity, this can be an enormous value. For instance, the temperature increase for silicon with thermal conductivity of 148 W/mK is < 2℃ even for very high doses. On the other hand, for polymers and biological materials with thermal conductivity of generally 0.1 W/mK this value is much higher[4].

1.4.2.5. Redeposition

From the perspective of thermodynamics, the sputtered atoms and ions, which are thrown out from the solid surface into the gas phase, are not in equilibrium. In case of any collision with nearby solid surfaces, the sputtered particles can be condensed back into the solid phase and a fraction of ejected atoms may crash back into the sputtered surface and redeposit on it[27] .

Different aspects of sputtered particles such as their charge, mass, kinetic energy and sputtering direction should be understood to prevent and control redeposition. It is also

noteworthy that the sputtering yield of target material and the geometry of milled pattern are key parameters in intensity of redeposition.

Still there are several methods to overcome this issue. Some of the most important ways are: using a protective layer, lowering the incidence angle of the encroaching Ga^+ ions, lowering the ion energies, and optimizing milling geometries. Another but not a common way to reduce the redeposition effect is using high atomic mass ions as ion beam source. As an example using In^+ instead of Ga^+[40] .

In TEM specimen preparation by FIB to prevent redeposition usually a low energy of ion beam polishing is conducted as the last stage with energies about 5 keV and currents around 70 pA.

1.4.2.6. Swelling

During FIB patterning, amorphization and ion implantation are two main factors of ion-induced swelling. However, the capability of these mechanisms is different based on the material. For instance swelling which occurs on crystalline semiconductors is the direct result of material amorphization, in this case ion implantation does not seem to markedly commit to volume expansion. The applied pressure from the crystal on the amorphized material cause the volume expansion towards the surface or swelling. At higher irradiation doses, the prominent process is surface erosion instead of swelling[41].

Frey et al[38] have shown that, although at low ion doses no material removal will be observed, but the implanted gallium would lead to swelling of the exposed area. Then, with the increasing dose, material removal will start. The material removal shows a dose-dependent behavior as plotted in figure 2.6 (c).

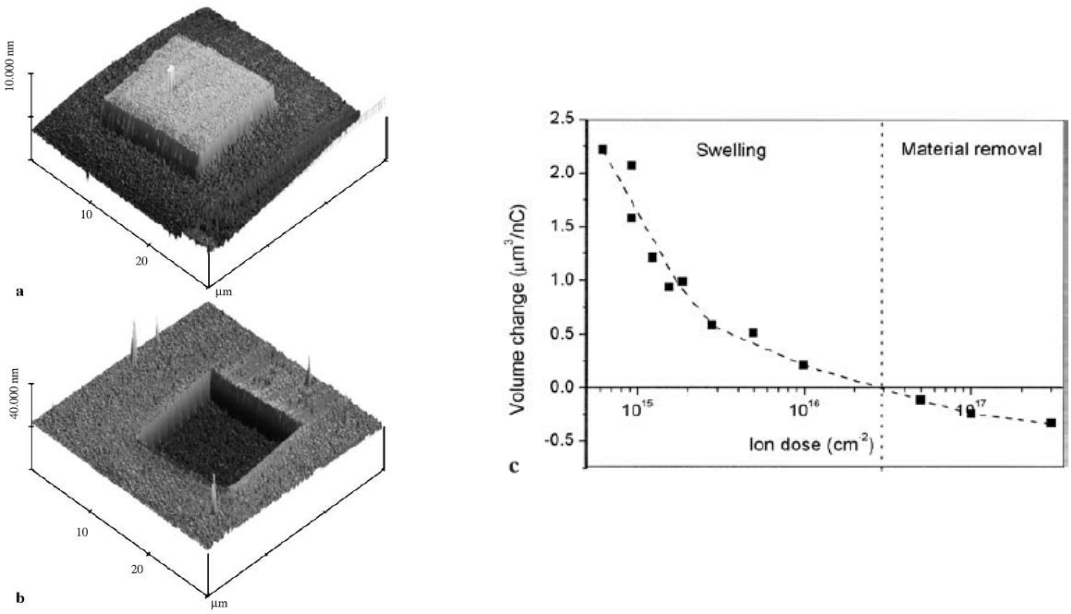

Figure 21 AFM measurement showing the swelling and material removal processes with respect to ion dose **(taken from[38])**

The participation of amorphization is more than ion implantation factor since the volume change caused by swelling is far way more than the volume of the implanted atoms. The swelling due to amorphization can be tens of nanometers and is an important deliberation in nanofabrication[27].

2. Material and Methods

2.1. Dentin and Enamel

The human tooth as one of the most important organs of human body can be detached to 2 distinct parts: the crown and the root. The part that involves in chewing food is known as crown. The root is the other region of human tooth, which is located under the gum line and anchors the tooth to a boney socket called alveolus. The outer surface of the root is capped in a bone-like combination of calcium and collagen fibers called cementum. The three major layers of each tooth are known as pulp, dentin and enamel (Fig. 22).

- *Pulp:* the soft combinational tissues in the central part of the tooth consists of a vascular region called pulp. There are tiny holes in the tip of the roots that the tiny blood vessels and nerve fibers enter to them in order to support the hard exterior regions.
- *Dentin* is a tough mineralized layer of tissue, which surrounds the pulp. Since the dentin is composed of collagen fibers and hydroxylapatite (a calcium phosphate mineral), it is much harder than the pulp. The nutrients produced in the pulp spread through the tooth by means of dentin due to the porous structure of it. The porous structure of dentin is the key property of it, which is widely studied in this work. Further detailed information will be given about dentin in subsequent sections (Fig. 23).
- *Enamel is* the hardest substance which can be found within human body. This nonporous material mainly made of hydroxylapatite and cap over the dentin. The other part of this study is about this hard material.

2.1.1. Dentin

Dentin is a hydrated hard tissue that comprises the majority of human teeth by both weight and volume[42]. The tissue serves as an elastic foundation for the hard, outermost enamel, and as a protective enclosure for the central pulp. Dentin consists of microscopic channels, called dentinal tubules, which radiate outward through the dentin from the pulp to the exterior cementum or enamel border. By increasing the distance from the pulp, the tubule density decreases within the dentin. A highly mineralized cylindrical cuff of apatite mineral encircled the tubules and is regarded as

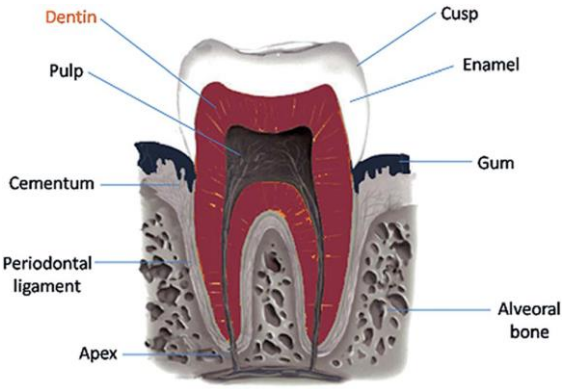

Figure 22 The scheme of a human tooth showing the individual layers

the peritubular dentin. Intertubular dentin employ the interstitial space between the peritubular cuffs and is consisted of a matrix of collagen fibrils that is bound by crystalline apatite. The collagen fibrils are dispersed in planes basically perpendicular to the lumens[43]. The tubules contain fluid and cellular structures[44]. As a result, dentin has a degree of permeability, which can increase the sensation of pain and the rate of tooth decay. Dentin is traversed by a network of tubules that are oriented radially outward from the central pulp towards the dentin–enamel junction[42]. On the other hand, type I collagen forms a fibrous threedimensional network structure which build up the dentin matrix. Compared to bone, the collagen matrix in dentin is more interwoven with numerous crossing of fibrils[45]. The tubule lumens are about 1 μm in diameter and are surrounded by a 0.5–1.5 μm hypermineralised layer of peritubular dentine (PTD) which seems to be non-collagenous[46].

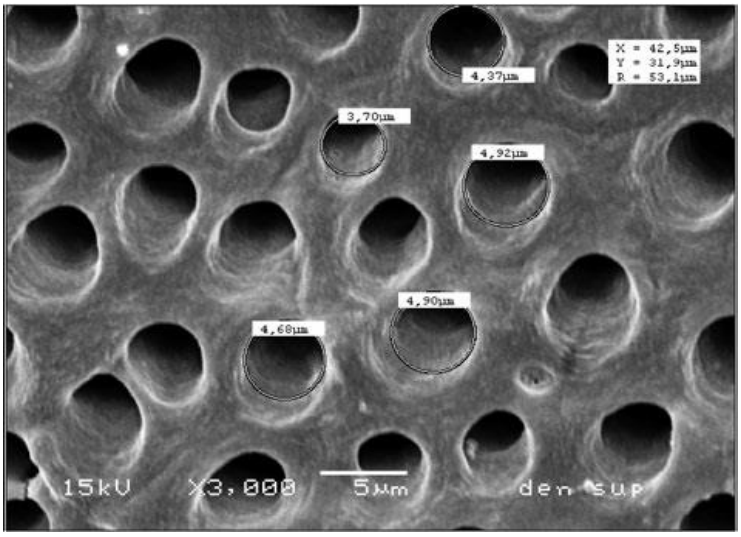

Figure 23 SEM micrograph showing dentinal tubules and porous structure of dentin **(taken from[47])**

2.1.2. Enamel

Enamel is the toughest biological texture in the human body and is a composite material comprised both a mineral and an organic phase. The mineral phase predominates (95–96 wt.%) and comprised calcium phosphate salts in the form of large hexagonal hydroxyapatite crystals that are both carbonated and defective. Sets of similarly orientated crystals form rod-like structures called enamel prisms, 3–6μm in cross-sectional diameter. Prisms are separated from each other by a thin organic prism sheath and by interprismatic enamel. The protein/organic matrix comprises approximately 1 wt.% of the enamel, and the remaining approximately 3 wt.% is contributed by water[48].

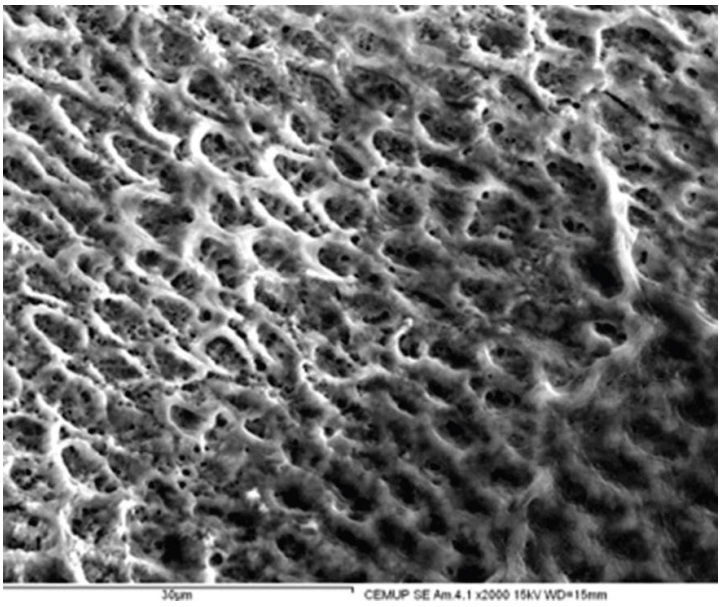

Figure 24 SEM image of enamel surface morphology after laser and phosphoric‑acid treatment **(taken from[49])**

2.2. Titanium dioxide (TiO2)

The TiO_2 has been commercially produced in the early twentieth century and has been widely used as a pigment[50] in ointments, toothpastes[51], paints[52] and sunscreens[53], [54]. Later in 1972 the photocatalytic splitting of water on a TiO_2 electrode under ultra violet (UV) light has been discovered by Fujishima and Honda [66-68]. Since then various applications have been developed for TiO_2 roughly categorized in two main "energy" and "environmental" groups moving over wide areas from photovoltaics and photocatalysis to photo-/electrochromics and sensors[55]–[57]. These applications based on both the properties of TiO_2 alteration of TiO_2 material. furthur, there is an exponential growth of investigations on nanoscience and nanotechnology[58].

Various properties of materials differ whit diminishing the size of material especially down to the nanometer range. These properties vary in the range of physical, chemical and mechanical properties. For instance, the specific surface area and surface to volume ratio boost drastically as the size of the material decline[59]. Additionally, TiO_2 is a promising material among photocatalyst materials, which may overcome many environmental, and pollution issues. Since most of the applications of TiO_2 relate to its optical properties many efforts have been done during past years to modify the optical properties of TiO_2. By doping it is possible to increase the optical sensitivity and activity of TiO_2 nanomaterials in the visible light region[58]. In this work, TiO_2 nanoparticles are doped with Ga^+ physically by means of Focused Ion Beam (FIB). There are various methods for synthesizing TiO_2 nanostructures. In this work TiO_2 in anatase phase from the Sigma-Aldrich company in the size of 25 nm has been used.

2.2.1. Properties of TiO_2 nanomaterials

2.2.1.1. Structural properties

TiO_2 exists in 4 main crystal structures: the stable rutile (tetragonal, a = b = 4.584 A, c = 2.953 A), metastable anatase (tetragonal, a = b = 3.782 A, c = 9.502 A), brookite (rhombohedral, a = 5.436 A, b = 9.166 A, c = 5.135 A) and TiO2 (B) (monoclinic, a = 12.16 A, b = 3.74 A, c = 6.51 A)[60]. Figure 24 represents the unit cell structure of rutile and anatase TiO_2. These two structures can be defined in terms of chains of TiO_6 octahedra, where each Ti^{4+} ion is encircled by an octahedron of six O^{2-} ions. The main differences between these two crystal structures are in the distortion of each octahedron and by the assembly pattern of the octahedra chains[58]. Whereas in rutile the octahedron is distorted slightly towards orthorhombic, in anatase, this distortion is significant in a way that its symmetry is less than orthorhombic. Additionally in anatase the Ti-Ti distances are larger and Ti-O distances are shorter than those in rutile. Table 1 shows the structural parameters of TiO_2[61]. In terms of assembly pattern each octahedron in rutile is in contact with 10 neighbor octahedrons (two sharing edge oxygen pairs and eight sharing corner oxygen atoms), as long as, in the anatase structure, each octahedron is in contact with eight neighbors (four sharing an edge and four sharing a corner). Between different polymorphs of TiO_2, rutile is the most stable phase for particle having a size higher than 35 nm[60] while this size for anatase to be thermodynamically stable is below 10–20 nm[60].

Table 1 srtuctural parameters of TiO2 **(taken from[61])**

Sample	Ti–O bond length (Å)	O–Ti–O bond angle
anatase	4 — 1.934 2 — 1.980	4 — (92.4°) 4 — (78.1°) 4 — (101.9°)
brookite	2 — 1.99 1.87, 1.92, 1.94, 1.95	77.2°, 80.1°, 80.1°, 85.3°, 87.1°, 89.2°, 93.7°, 93.8°, 95.1°, 96.1°, 97.3°, 104.8°
rutile	4 — 1.949 2 — 1.980	2 — (98.8°) 2 — (81.2°) 8 — (90.0°)

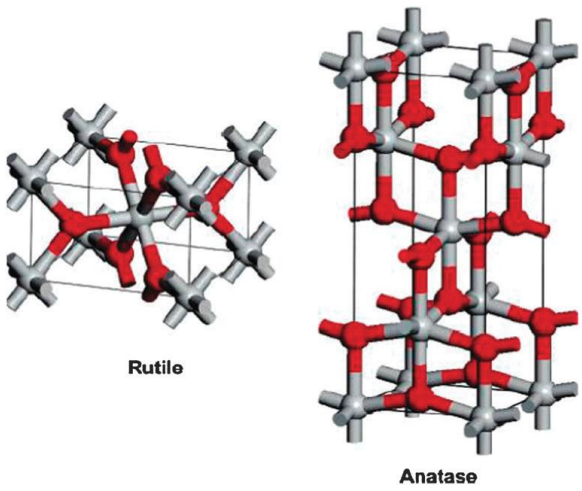

Figure 25 TiO_2 crystal structure comparing two distinct phase of rutile and anatase **(taken from[60])**

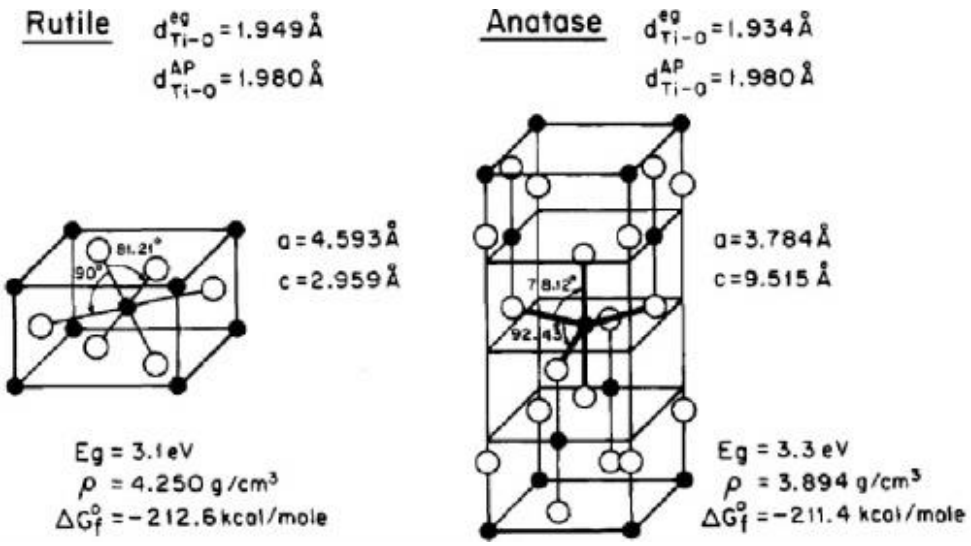

Figure 26 TiO2 crystal structure with detailed information **(taken from[58])**

2.2.1.2. Raman vibration properties

There are six Raman scatters assigned to anatase TiO_2 in the vibrational spectrum: three Eg modes located around 144, 197, and 639 cm^{-1} (entitled here Eg(1), Eg(2), and Eg(3), respectively), two B1g modes at 399 and 519 cm^{-1} (entitled B1g(1) and B1g(2d)), and an A1g mode at 513 cm^{-1}. The modes of Eg(3) B1g(2) and A1g are the Ti-O bond stretching type vibration and on the other hand, the modes of B1g(1), Eg(1) and Eg(2) are the O-Ti-O bending type vibration[62]. Generally, with decreasing the size of TiO_2 nanomaterial the featured Raman scattering peaks become wider. Various factors may result in the size effect on the Raman scattering in nanocrystalline TiO_2 such as phonon confinement, nonstochiometry, or internal stress/surface tension effects. However the most convincing theory among these theories is 3 dimensional phonon confinements in nanocrystals. Heightened widening and systematic frequency deviations in Raman peaks can be observed as the particle size declines. The maximum blue shift and serious widening are found in the most intense Eg(1) mode with deteriorating crystallite size. A small blue shift is observed for the Eg(2) mode, while the B1g(1) mode and the B1g(2)+A1g modes show very small blue shifts and red shifts (the latter peak performs a combined effect of two individual modes), respectively. Whereas the frequency shifts for the A1g and B1g modes are not distinct. For these modes as the it can be seen with declining the crystallite size the peaks become wider. The Eg(3) mode shows severe widening and a red shift with declining crystallite size[58].

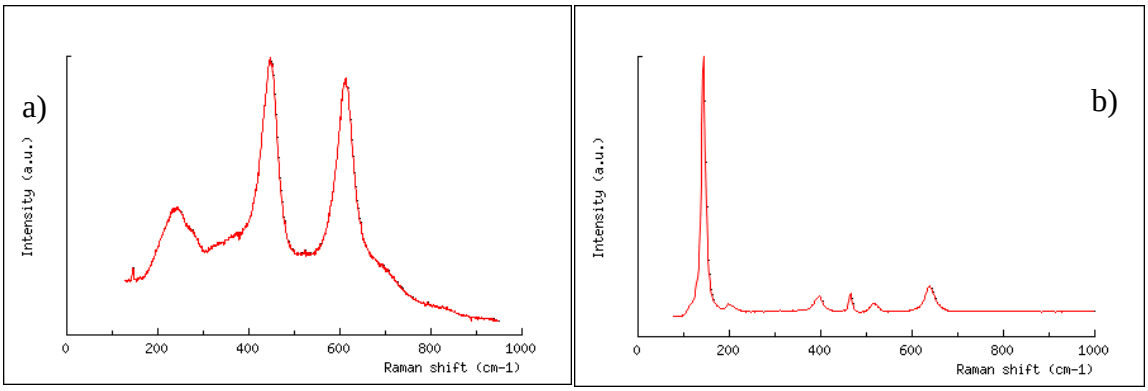

Figure 27 Raman spectra of nanoparticle TiO2. a) rutile b) anatase

2.3. Characterization and Analysis

2.3.1. Focused Ion Beam (FIB)

As already mentioned in the earlier chapters, dual beam systems have great range of capabilities for various application fields in science. Although in the last decade, dual beam systems have mainly been serving for semiconductor technologies, which were based on inorganic materials, but nowadays FIB is a popular instrument for different materials even for organic materials. In this thesis study, a large spectrum of dual beam applications was applied on human dentin, enamel and on TiO_2 anatase.

The major part of the experimental work of the study was carried out by a dual beam FIB system, which enabled the use of electron and ion beam applications in one instrument. A JIB 4601F system from Jeol Company and a LYRA3 system from Tescan Company were utilized for a large portion of the experiments.

Both the Jeol JIB 4601F and Tescan LYRA3 dual beam instruments have a Schottky FEG electron source which provides a resolution down to 1 nm at 30 keV electron energy and a gallium liquid metal ion source with a minimum resolution of 10 nm at 30 keV ion energy. An Everhart-Thornley detector was mainly used for imaging, where high resolution images were acquired by In-Beam detector, which is an annular in-lens detector, placed in the electron column. The In-Beam detector is a scintillator type of detector, which uses secondary electrons generated by the primary beam to produce an image. Since it is mounted within the lens, the collected electrons are the ones from immediately over the scanned area of the sample. The electrons must travel through the lens pole piece into the collector, hence the name In-Beam detector. In this study the slice and view technique for 3D reconstruction of human dentin and also TEM sample

preparation of human dentin performed with Jeol JIB 4601F equipped with OmniProbe as a micromanipulator. The TiO2 anatase surface irradiation was performed by LYRA3 Tescan dual beam instrument.

2.3.2. Scanning Electron Microscopy (SEM) and Energy Dispersive X-ray Spectroscopy (EDXS)

In this study, with along electron columns in the dual-beam FIB systems, an Energy Dispersive X-ray detector (EDS detector) was used to quantify the amount of gallium implantation on TiO_2 anatase surface. The investigation was performed with an Oxford X-Max Silicon Draft Detector (SSD) with the size of 150 mm^2 and for interpretation of collected X-rays Aztec Energy EDS Microanalysis software was used.

2.3.3. Raman Spectroscopy

One of the main spectroscopies employed for analyzing various materials are based on the process of Raman scattering. This technique is broadly used in order to get data of the chemical structures of materials to identify object from characteristic spectral patterns (fingerprints). By means of raman spectroscopy it is almost possible to resolve the amount of a substance in a sample quantitatively or semi quantitatively. Raman spectroscopy is a molecular based spectroscopy, which employs the inelastically scattered light. In this technique, vibrational states of molecules (phonones) interrogated and identified. For this reason, Raman spectroscopy not only is a priceless cogent tool for molecular detection, but also provides useful data about molecular bond structure modifications (e.g. state changes and stresses & strains). It is not the only member of vibrational spectroscopy family. Besides this method, there are also other methods such as FT-IR and NIR but Raman has assorted benefits over them. This is because the Raman Effect exhibits in the light scattered off of a sample as opposed to the light absorbed by a sample. This fact cause almost no sample preparation for Raman spectroscopy investigation and is insensitive to aqueous absorption bands. Therefore, this property enables Raman to investigate wide variety of materials in the range of solids, liquids, gases both directly or through a transparent container such as glass, quartz and plastics. One of the significant advantages of Raman spectroscopy is the fact that this technique is highly selective and can identify and differentiate molecules and chemical species that are very similar. As an example TiO_2 has two different phases with similar structures (Rutile and Anatase) however the Raman featured scattering peaks are very different as shown before. For

another instance as shown in Figure 27 Raman spectroscopy of five similar molecules (Ethyl Acetate, Ethanol, Acetone, Tolune and Dimethyl Sulfoxide) were given. It is apparent that their Raman spectra is completely different even for untrained eye although they have same molecule structure. In addition we can use Raman spectral libraries to identify or verify wide variety of materials.

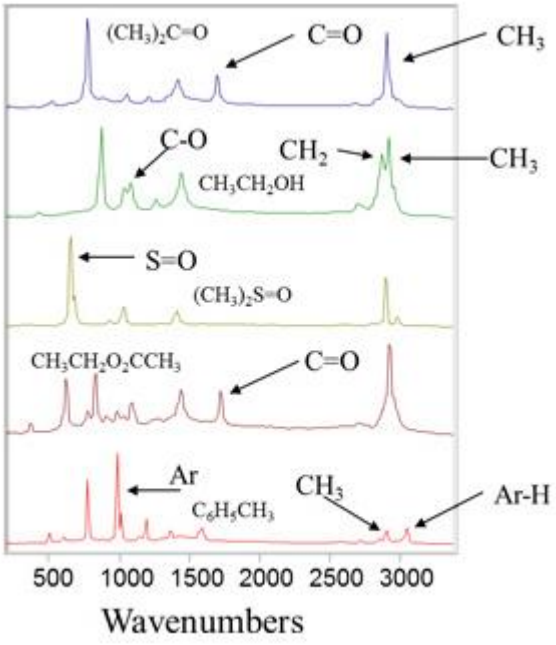

Figure 28 Example Raman spectra of various molecules **(taken from[63])**

There are two ways to physically interpret the Raman scattering: with the classical point of view, which says light, is a wave or from the quantum perspective which defines the light as particle. In the classical wave interpretation, light can have an interaction with a molecule through its polarizability. This is a result of electromagnetic radiation behavior of light, which contains an oscillating electric field. Polarizability is determined by the electron cloud's ability to interact with an electric field. For this reason there is a huge difference between soft and hard materials in terms of Raman scattering, while the Raman scatters are strong in soft molecules such as benzene. In case of tougher molecules such as water, they apt to have a moderate weak Raman scatters. On the other hand, in quantum, particle interpretation light is not a wave anymore and consider being a photon, this particle hits the molecule, and then inelasticaly scatters. In this case, the size of the bond has a proportionality with number of scattered photons. So here, Pi bonds play a crucial role in scattering process in such a way that molecules like benzene which obtain

a large Pi bonds apt to scatter profuse photons, as long as water which is a molecule that obtain small single bonds have a weak Raman scattering effect.

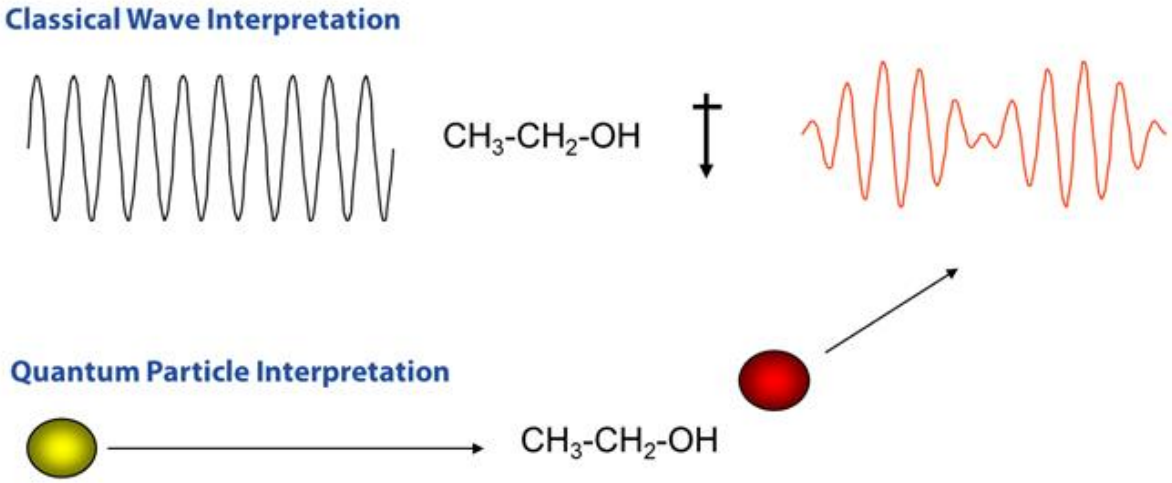

Figure 29 Comparison of Raman scattering interpretation **(taken from[63])**

Assimilation of a simple diatomic molecule as a mass on a spring may help us to have a better understanding of the Raman effect. According to Figure 30 *m* is the atomic mass, *x* is the displacement, and *K* serves as the bond strength.

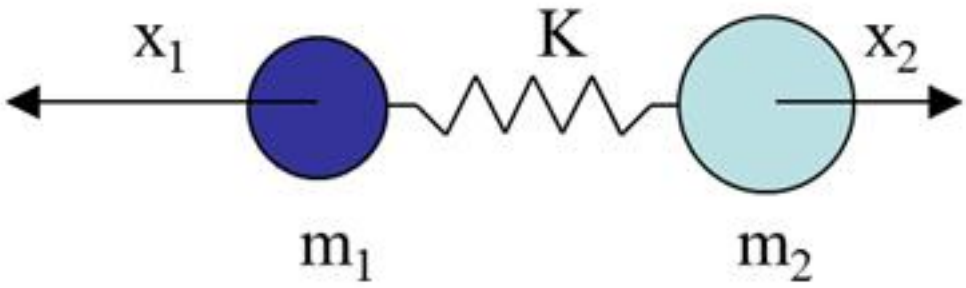

Figure 30 Schematic showing the model of diatomic molecule as a mass on a spring **(taken form[63])**

Now it is feasible to use the Hooke's law in order to express the displacement of the molecule (Eq1).

$$\frac{m_1 m_2}{m_1+m_2}\left(\frac{d^2x_1}{dt^2}+\frac{d^2x_2}{dt^2}\right)=-K(x_1+x_2)\,.$$

Equation 1

By substitution of the reduced mass (*m1m2/[m1+m2]*) with μ and the entire displacement (*x1+x2*) with *q*, the equation can be written in a concise shape of:

$$\mu \frac{d^2q}{dt^2} = -Kq,$$

Equation 2

By figuring out this equation for *q* we get,

$$q = q_o \cos(2\pi \nu_m t),$$

Equation 3

where ν_m is the molecular vibration and its formula is,

$$\nu_m = \frac{1}{2\pi}\sqrt{\frac{K}{\mu}}.$$

Equation 4

From equations 3 and 4, it is obvious that there are two parameters involving with molecule vibration pattern. This function is a cosine function with a frequency proportional to the bond strength and inversely proportional to the reduced mass. From this we can conclude that there is a unique vibrational fingerprint for each molecule which are determined both with atoms in the molecule and the characteristics of the individual bonds. The relationship between polorizability and displacement makes the Raman effect a reasonable tool for measuring the vibrational frequencies. The dipole moment *P* induced by the interaction of photon and the molecule equals to that of the product of the polorizability of the molecule and the electric field of the incident light source. This can be shown as,

$$P = \alpha E_o \cos(2\pi \nu_o t),$$

Equation 5

Here E_o is the intensity and v_o is the frequency of the electric field. It is reasonable to say that the polorizability is a linear function of displacement using the small amplitude approximation.

$$\alpha = \alpha_o + q\left(\frac{\partial \alpha}{\partial t}\right)_{q=0} + \cdots,$$

Equation 6

which when combined with equations 3 and 5 results in,

$$P = \alpha_o E_o \cos(2\pi \nu_o t) + q_o \cos(2\pi \nu_m t)\, E_o \cos(2\pi \nu_o t)\left(\frac{\partial \alpha}{\partial t}\right)_{q=0}.$$

Equation 7

the two distinct results of the molecule and the incident light interaction are Rayleigh and Raman scattering. Among these two kind of scattering the Rayleigh scattering is the prominent one which results in no shift in the frequency of the incident light. But when the Raman effect component in the equation expanded to,

$$q_o E_o \left(\frac{\partial \alpha}{\partial t}\right)_{q=0} [\cos(2\pi\{\nu_o - \nu_m\}t) + \cos(2\pi\{\nu_o + \nu_m\}t)],$$

Equation 8

cause a shift in the frequency of the incident light by plus or minus the frequency of the molecular vibration. Depending on decreasing or increasing in frequency this shift can be categorized into two distinct group of Stokes shift and Anti-Stoke shift respectively. Nowadays it is possible to directly measure the shift in frequency from the incident light (normally, only the Stokes shift is utilized for this measurement) which provides the vibrational frequency of a molecular bond. However, quantum particle interpretation gives a better view of the process. As mentioned before the Raman Effect is the consequence of inelastic scattering of a photon when it hits a molecular bond. From the Jablonski diagram shown in Figure 30. We can see that the hitting photon excites the molecule into a virtual energy state.

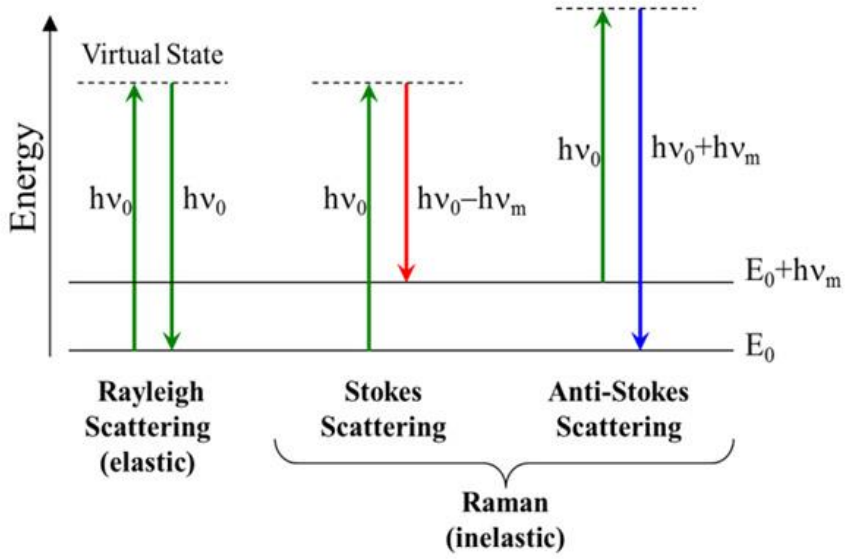

Figure 31 Jablonski diagram representing the transitions for various scattering **(taken form[63])**

There are three possibilities when this phenomenon occurs. The first procedure occurs when the energy of the emitted photon is equal to the energy of incident photon which can be categorized as Rayleigh scattering with no energy lose during the process. In the second case the emitted photon has lower energy compare to that of the incident photon; this is known as Stokes shifted Raman scattering. The third outcome occurs whit a molecule in an excited phonon state. When this molecule excites to a higher virtual state, and then relaxes back down to the ground state the emitted photon has higher energy compare to that of the incident photon; this is known as Anti-Stokes Raman scattering. However, this third potential outcome is rare since most molecules are in the ground state at room temperature. The decreased population of the excited vibrational states causes the anti-Stokes scattering to be weak compare to Stokes scattering. Additionally, with increasing the temperature anti-Stokes scattering increases respective to Stokes scattering. Each compound has its own unique Raman spectrum, which can be used as a fingerprint for the identification of the substance. Typically, the stoke scattering in the low energy side is used to record the Raman scattering however we should have in our mind that infrequently anti-Stokes scattering is favoured. For instance, the anti-Stokes scattering sometimes is used to avoid fluorescence interference. With additional examination of the quantum explanation of the Raman effect, this result can be drawn:

the power of the scattered light, P_s, is equal to the product of the intensity of the incident photons, I_o, and a value known as the Raman cross-section, σ_R. It can be shown that,

$$\sigma_R \propto \frac{1}{\lambda^4},$$

Equation 9

where λ equals the wavelength of the incident photon. Therefore,

$$P_s \propto \frac{I_o}{\lambda^4}.$$

Equation 10

Equation 10 shows the relationship between the power, the light intensity and the wavelength of it. In addition, these equations also show that using a short excitation wavelength can be desirable most of the times and a high power excitation source is also desirable.

The change in the polarizability of the electron cloud round the molecule is a direct result of Intense Raman scattering which occurs from vibrations. The greatest scattering is typically results from symmetric vibrations. This is exactly in contrast with infrared absorption where the asymmetric vibrations play the dominant role in formation of intense scattering where the most intense absorption is caused by a change in dipole. In a centro-symmetric molecule, no band can be active in both Raman scattering and infrared absorption. The typical vibration occurs sinusoidally with a frequency ν which is a combination of changes in the positions of atoms in the molecules.

Stretching: a change in the length of a bond, such as Ti-O or C-C.

Bending: a change in the angle between two bonds, such as the HCH angle in a methylene group.

Rocking: a change in angle between a group of atoms, such as a methylene group and the rest of the molecule.

Wagging: a change in the angle between the plane of a group of atoms.

Twisting: a change in the angle between the planes of two groups of atoms.

Out-of-plane: it can be described in BF3 as an example when the boron atom moves in and out of the plane of the three fluorine atoms.

According to the definitions there is no change in the angles and bond lengths within the groups, in a rocking, wagging or twisting. Rocking may be dignified from wagging by the fact that the atoms in the group stay in the same plane. Since Raman is a form of vibrational spectroscopy, energy transitions arise from molecular vibrations. Because these vibrations involve identifiable functional groups, they can be used to identify the molecular, if the energies of these transitions are plotted as a spectrum. The table shows characteristic Raman vibrational frequencies of organic groups.

All Raman spectrometers have three major components: a detector, a sampling apparatus, an excitation source. The excitation source in modern Raman instruments usually is a laser due to its ability of proiding a coherent beam of monochromatic light. This provides adequate intensity to produce a reasonable load of Raman scatter and allows for spectra with minimum noise. For the detector it is usually a spectrometer, and for the sampling apparatus, it can be either a microscope or a fiber optic probe. It is extremely important to have a monochromatic excitation source since Raman spectrometer measures a shift in wavelength (or frequency). In addition, the laser, as excitation source, should have an extremely stable frequency and does not mode hop. It is also indispensable to make use of a clean, narrow bandwidth laser since the quality of the Raman peaks is straightly impressed by the sharpness and stability of the excitation light source. Wavelength is another parameter, which is important in choosing a proper laser source. Normally the most powerful Raman signals obtains from the lights with short wavelength. Nevertheless, when working with organic materials this should not be the only consideration, since during the excitation of most organic molecules via high-energy (short wavelength) photons these molecules tend to fluoresce . Overwhelming the signal of fluorescence with Raman spectrum is inevitable, although it is a low light level process. The result of this lies in the fact that the Raman Effect is consisted of a very tiny fraction (about 1 in 10^7) of the incident photons.

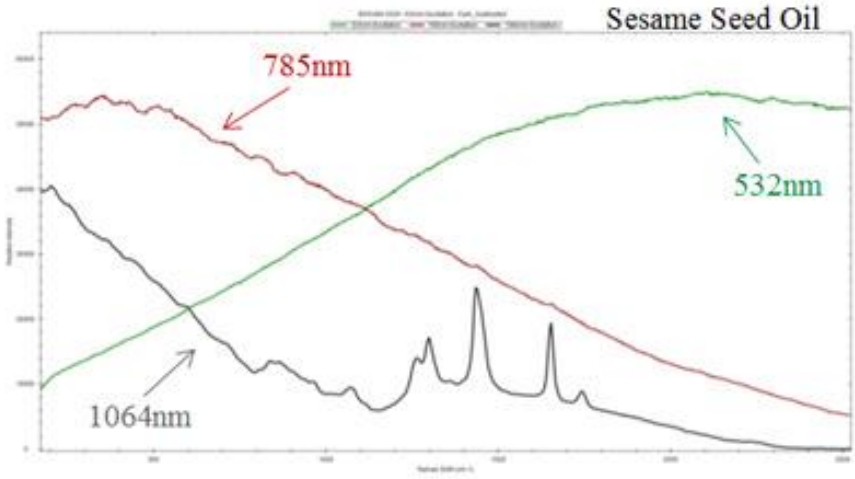

Figure 32 Comparison of raman spectrum at various excitation wavelengths **(taken from[63])**

The most convenient laser to have a maximum fluorescence contraction without cede of spectral range or resolution is 785nm diode laser. However, in order to have heightened sensitivity for inorganic molecules, a 532nm laser is the best superior since fluorescence is not a problem anymore. Allocating long collecting times in order to collect sufficient photons to measure a detectable signal is unavoidable since the Raman scattering is very weak. In order to reduce the dark noise, it requires using a TE cooled spectrometer. For even lower concentrations or weak Raman scatters, utilizing a back-thinned CCD for boosting the sensitivity of the spectrometer can be helpful. According to Beer's law, it is probable that the detector reabsorbs the electron as it goes through it. For avoiding this problem, it is necessary to etch the detector to only a few microns thick. This improves the detector's sensitivity from a maximum quantum efficiency of 35% to more than 90%. It is probable that the Raman spectra contain peaks, which are fairly close together. This is because of the highly selective nature of Raman spectra. Most of the times with respect to the application it is imperative to separate these nearly spaced peaks. This is possible with a high-resolution spectrometer. Usually there are available options of different custom excitation wavelengths other than 532nm and 785nm laser excitation wavelengths. This spectral range usually available from $65cm^{-1}$ to $4000cm^{-1}$with a spectral resolution as fine as $3cm^{-1}$.

The most effective way to direct the laser light to the specimen and accumulate the Raman scatter and again directing it to a spectrometer is fiber optic probe. A Raman probe should fulfil three main functions: firstly, directing and focusing the monochromatic excitation source (typically a laser) to the sample. Second accumulating the scattered light and finally directing it to the spectrometer.

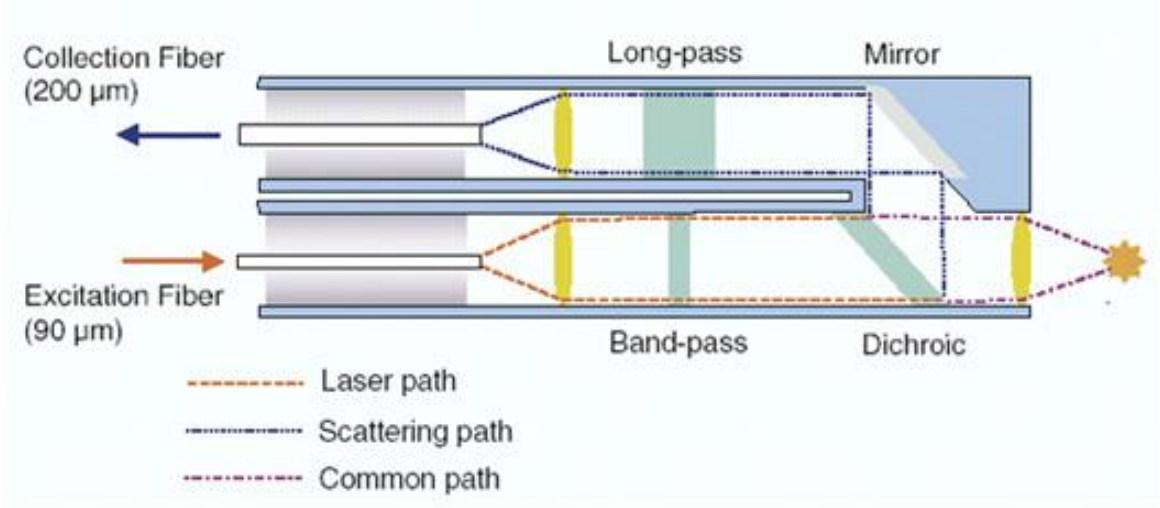

Figure 33 Typical Design of a Raman Probe **(taken from[63])**

Prior to reaching the light to the sample a narrow band-pass filter located in the optical path of the excitation source, due to the significance of every pure signals in Raman spectroscopy. It is also extremely important to collect the data in 0^o angle normal to the sample. The reason for this is avoiding the interference of Rayleigh scattering by means of a filter before it is directed to the spectrometer. The use of fiber optics makes it easy to do Raman investigation on different materials from a solid sample as well as liquids or in both laboratory and process environments (for real time kinetic measurements).

In this study, Raman spectroscopy was the major characterization technique used for the determination of TiO_2 anatase phase transformation, amorphization and oxygen vacancies production caused by ion beam irradiation. All Raman measurements were perforemed on a Raman Renishaw InVia System attached with 532 nm green laser and 2400 lines/mm grating.

2.3.4. Transmission Electron Microscopy (TEM)

Transmission Electron Microscopy (TEM) is a facility, which image the sample with the electrons that passing through a very thin specimen. Due to transmission of electrons

through the sample diverse electron-specimen interactions may occur. The formed image magnified and focused by an objective lens and can be appear with various tools such as an imaging screen, a fluorescent screen plus a monitor, or a layer of photographic film, or by a sensor such as a CCD camera[64].

TEM can give information about the microstructure, crystal quality and defect concentrations in a device or a layer. In addition, diffraction pattern can provide information about the crystal symmetry and lattice parameters data. Moreover, there are various techniques such as energy dispersive X-ray analysis, Auger spectroscopy and Electron Energy Loss Spectroscopy (EELS) for obtaining compositional information of the specimen.

Another application for TEM is providing information about the thickness of each layer in multilayer specimens as well as their composition and the quality of the interface between the layers. It may also reveal the extended defects such as dislocations and stacking faults.

In the current study in order to track the nano-sized features within the dentin and enamel structure, such as collagen fibrils, the sample was investigated in TEM. Due to the difficulties of site-specific sample preparation from hard materials by other methods, the TEM specimen preparation process was also carried out by the help of a dual-beam platform. These pin-like thin samples were investigated in a FEI TF30 HR-TEM system and BF images were acquired at 300 keV electron energy.

3. Experimental Results and Discussions

In this part of the thesis, all results from the experimental study including evaluation of data and images will be presented. Besides, bringing together all the results concerning 3D reconstruction and Electron Tomography reconstructing of human dentin and enamel, the ion beam irradiation effect on TiO_2 anatase will be discussed and presented.

3.1. 3D image Reconstruction of human dentin via slice and view technique

As we mentioned in earlier chapters dual beam instrument has the ability to provide three-dimensional information methodologies in order to achieve truly quantitative materials characterization. The basic principle for 3D tomography is collecting continuous 2D data from the surface of the bulk material by serial sectioning and combining them into a 3D volume by means of several computational processes. Serial sectioning is applied by creating a planar surface by means of material removal via ion milling. For 3D image reconstruction, an area of interest is chosen and ion milling is used to devise a trench around the desired region with high beam currents (5-20nA). The trenches must be in a rescannable size to avoid redeposition of sputtered material and exclude shadowing of imaging signals. A protective platinum layer (about 1 μm thick) is deposited on surface aspect of the desired region before trenching to avoid Ga^+ implantation. After these steps, serial-sectioning process can be initialized. In this study before electron microscopy investigations, a human tooth was mechanically cross-sectioned with a die for a better view of layers within the structure. As shown in Figure 34, the tooth was channel treated and had fillings in the channels nearby dentin layer. In order to do 3D micro structural investigation by means of slice & view based tomography, the region of interest was chosen as the area marked by Yellow Square in the figure. Prior to dual-beam applications on the sample, in order to avoid charging effects that are caused by electron beams, the sample was gold-plated using a sputter coater. The thickness of gold coating was approximately 10 nm.

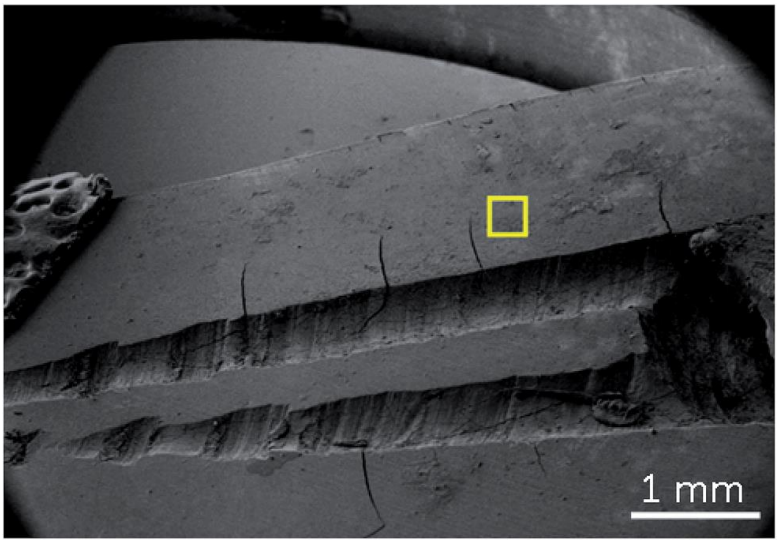

Figure 34 SE image showing the human tooth and the dentin layer around the channels. The selected areawith the yellow square shows the region where the FIB sectioning was done. The FIB tomography carried out on the region has dimensions of x = 18 μm, y = 17 μm and z = 16 μm

For the FIB slice & view series and the following 3D image construction a region of approximately 18×17×16 μm was chosen. Within this region, via ion milling, 332 slices were cut with a 50 nm step, using 1 nA ion current at 30 keV ion energy. The secondary electron (SE) images of the slice & view series was acquired at 2500× magnification simultaneously from the cross-sectioned regions. Next step is processing the related SE images using Stack N Viz software in order to achieve a 3D reconstructed tomograph. The major advantage over other imaging methods is the ability to track the features within the dentin 3D space. The results in this section provide the following information: the tubule distribution, alignment and orientation within the structure, which is available by, slice and view technique in dual beam platform. The different images of dentinal tubules distribution are shown in Figures 34 and 35. The mean number of tubules inside a 342 mm^2 surface for 332 slides is about 13. This gives a number for the tubular density of approximately 33000 consistent, with previous 2D studies. However, 3 dimensional observation makes it much easier to examine the tubule number densities. In addition, with cross sectioning technique we revealed the prisms as interior feature of human enamel as shown in Figure 37.

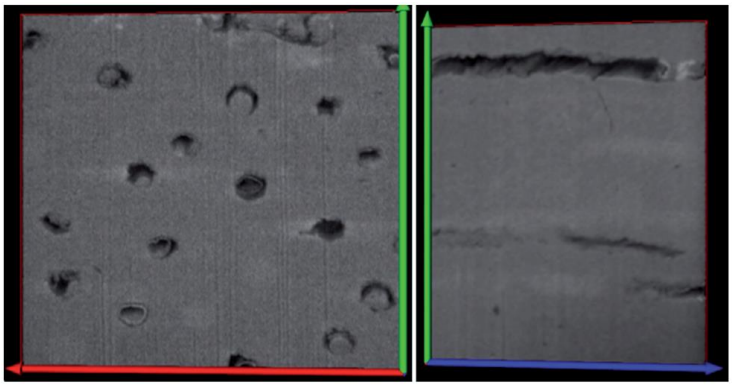

Figure 35 The SE images showing the distribution and alignment of the tubules for 3 axes: red arrow correspond to x axis, whereas blue arrow represent the y-axis and green arrow the z axis. The image on the left hand side shows the cross-sections of the tubules along the y axis and the image on the right hand side shows the tubules along the x axis.

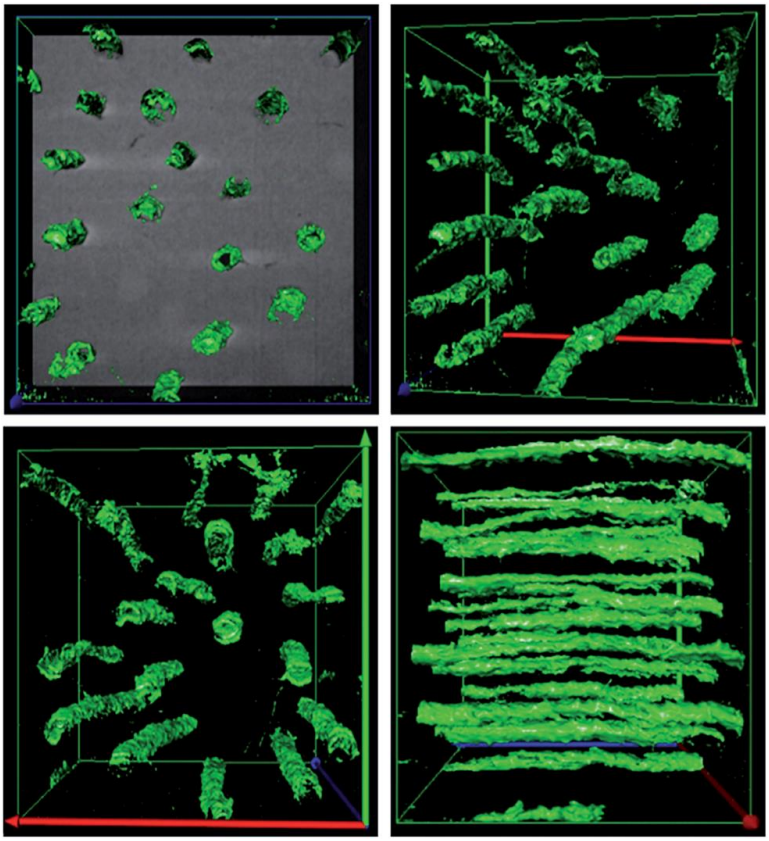

Figure 36 The 3-D reconstructed of dentin showing the tubule distribution in 3 dimensions: red arrow correspond to x axis, whereas blue arrow represent the y-axis and green arrow the z axis. For the reconstruction Stack N-Viz software was used.

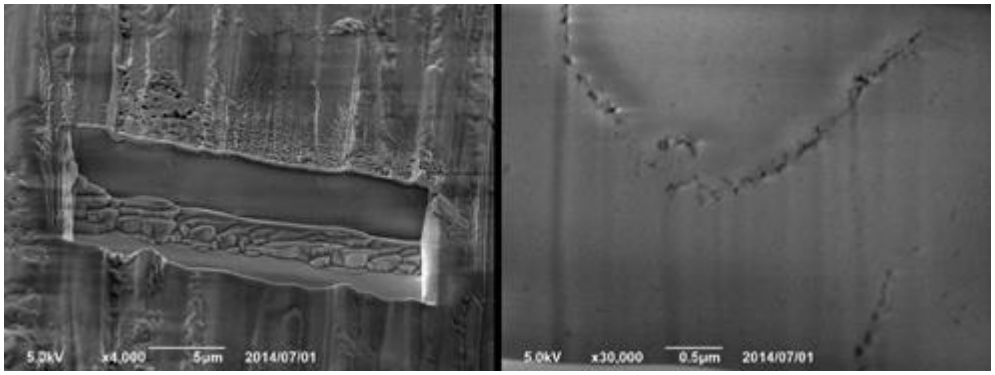

Figure 37 SE images showing the FIB cross-section of the enamel layer: the cross-cut on the surface and magnified SE image for observing the prisms.

3.2. Electron Tomography of human dentin and enamel

In order to track the nano-sized features within the dentin structure, such as collagen fibrils, the sample needed to be investigated in TEM to do the further electron tomography investigations. For revealing the nanosized 3D morphology of the material we can use Electron tomography (ET) technique as a direct method. It has proven to be a priceless tool in order to investigate the nanoparticles. The procedure starts with acquiring a series of projection images in a transmission electron microscope (TEM) by changing the tilt angle of the sample with respect to the electron beam. Then, aligning the acquired tilt series accurately for obtaining a high quality reconstruction. Fiducial markers are usually used for this reason. The procedure continues by backprojection of the aligned tilt series to form a digital three dimensional micrograph of the sample. As a last optional step, we may determine the different quantitative data by subjecting the reconstructed volume to a segmentation process. In this case the reconstructed volume is subject in order to segregation of the volume into specific objects of interest[65]. In ET, the direct model can be formulated as:

$$A.x = b$$

Equation 11

Here A is the projection matrix, $\boldsymbol{x}$ is the vector containing the voxels of the 3D object and $\boldsymbol{b}$ is the vector containing the pixels of the 2D projections. To reconstruct $\boldsymbol{x}$, an algebraic reconstruction such as Simultaneous Iterative Reconstruction Technique (SIRT) is often used in ET due to its reliability. A SIRT is actually a classical steepest descent algorithm minimizing the residual error. The initialization of this well-known algorithm starts with $\boldsymbol{x}^{(0)}=0$. At each iteration k, the solution $\boldsymbol{x}^{(k)}$ is updated according to the formula:

$x^{(k+1)} = x^{(k)} – \lambda^{(k)} A^{T}. (A.x^{(k)}-b)$

Equation 12

In Equation 12, A is applied to a volume $\boldsymbol{x}^{(k)}$ and is equivalent to a forward projection while A^{T} is applied to a set of projections and is equivalent to a back-projection. The relaxation parameter $\lambda^{(k)}$can be fixed or changed at every iteration.

The tilt series are usually acquired by High-angle annular dark-field scanning TEM (HAADF-STEM) imaging, since using this imaging technique underrate diffraction contrast, which contravene the projection requirement. It means we should have a specific physical property in order to have a certain contrast (mass/thickness in conventional TEM or Z^2 in HAADF-STEM). Due to the difficulties of site-specific sample preparation from hard materials by other methods, the TEM specimen preparation process was also carried out by the help of a dual-beam platform. The specimen preparation process in the dual-beam platforms was performed using in situ lift-out technique by the help of a micromanipulator. In order to prevent gallium implantation, initially two protective platinum layers were deposited on top of the region of interest before trenching with annular patterns. The free sections were then mounted on a TEM grid and thinned further by ion milling until thin samples (around 100 nm) were formed. In the final stage, TEM samples were polished, using rather low ion currents for the removal of gallium, which might have been implanted on the specimen surface during the milling process. As a result, electron transparent and uniform pin-like specimens were achieved. The uniformity of pin-form geometry provides detailed morphological and information in three dimensions (3D) while it is possible to acquire 3D data for revealing the collagen fibrils within the dentinal tissues. The SE images corresponding to the stages of pin-like TEM specimen preparation are given by Figure 38. The preparation steps can be summarized as following: (a) the deposition of protective electron beam assisted platinum layer (with a diameter of 5 μm) onto the region of interest; (b) the deposition of protective ion beam assisted platinum layer (with a diameter of 5 μm) onto the top of electron beam assisted deposit; (c) ion milling of pillar shape sections using intermediate ion beam currents (e.g. 0.1–1 nA) within annular patterns (the yellow circle corresponds to the annular pattern); (d) the lift-out of the section from the dentin structure using a micromanipulator; (e) mounting the pillar to the TEM grid using micromanipulator and

platinum deposition; (f) final thinning of the sample using low ion currents (e.g. 10–100 pA).

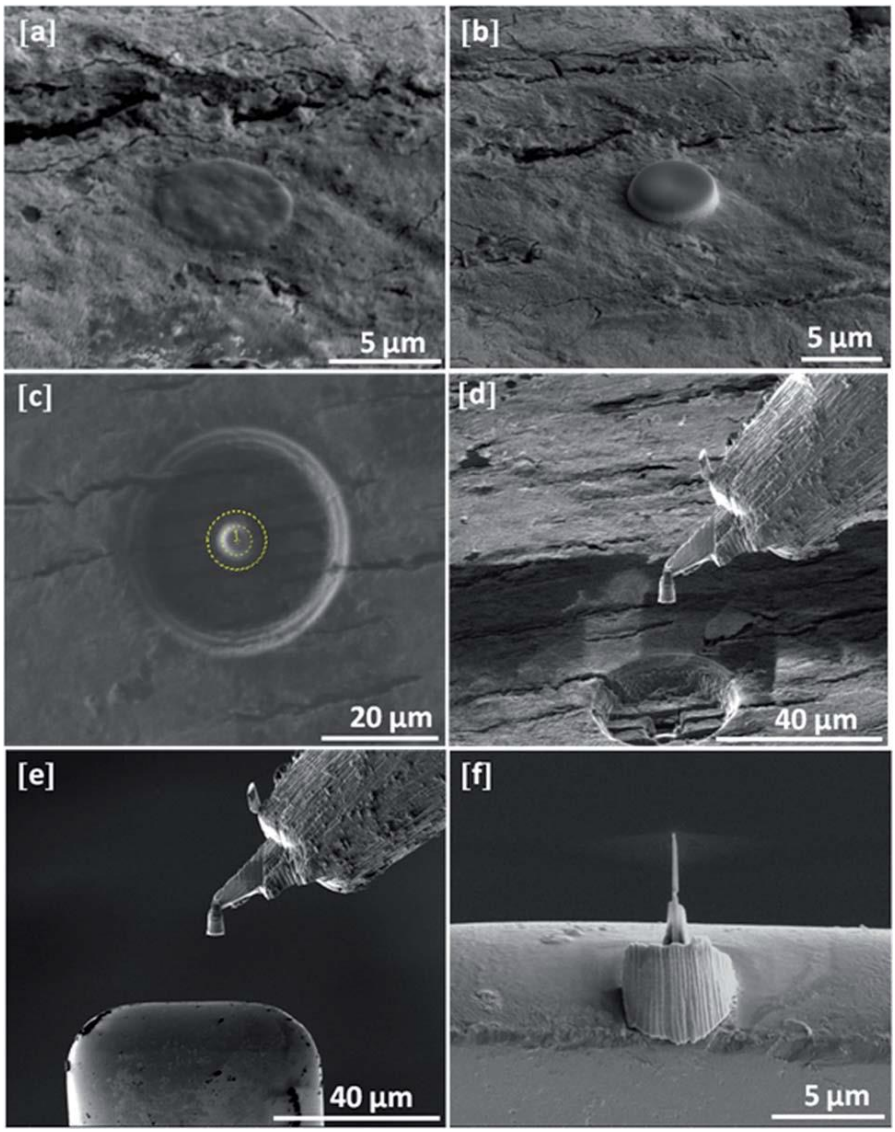

Figure 38 The steps for preparation of pin-like TEM sample using the dual-beam instruments: (a) deposition of electron beam assisted Pt layer, (b) deposition of ion beam assisted Pt layer, (c) ion beam milling via annular patterns, (d) lift-out of the pre-section, mounting of the pre-section onto the grid; (f) final thinning and polishing.

The TEM micrographs revealed the 3D network of collagen fibrils within the dentin structure. The corresponding micrographs are given in Figure 39. Transparent and normal dentin intertubular mineral crystallites appeared needle-like in morphology when observed on edge, similar to previous observations of dentin by other groups[66], [67]. Thus, the TEM analysis revealed the nano-features e.g. collagen fibrils that are present in the dentin structure, while the FIB work was useful for tracking the microsized features such as dentinal tubules. It should be noted that, FIB was the main instrument used for

the micro/nanomachining of both structures: tomography sections on the material and the pin-like TEM specimen. On the other hand, the TEM micrographs acquired from the enamel structures which were also prepared as pin-like samples showed a completely different morphology when compared to dentin structures. The crystalline structure was revealed by TEM while no significant porosity in nano or meso-scale was observed. The corresponding images are shown in Figure 40.

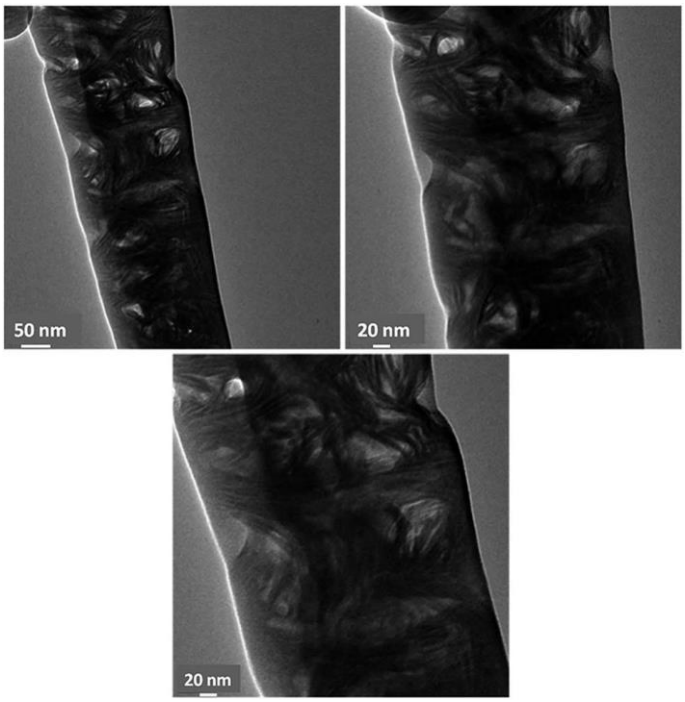

Figure 39 The Bright Field (BF) TEM images showing the 3D distribution of collagen fibrils within the human dentin. The micrographs show the nano features within the dentin structure.

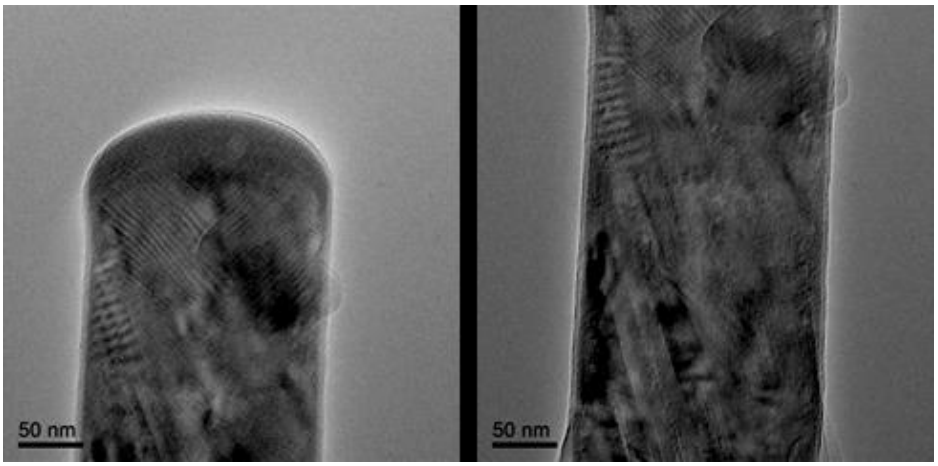

Figure 40 The Bright Field (BF) TEM images showing the crystalline structure of human dentin.

3.3. Ion Beam irradiation effects analysis on nanophase TiO_2 anatase in FIB

This section of the experimental work concerned the investigation of ion beam irradiation effects on nanophase TiO_2 anatase, in terms of phase transformation, amorphization, gallium implantation and production of oxygen vacancy. The experiments were carried out on compacted anatase nano powder with a diameter of roughly 1 cm.

For this experiment series, the sample surface was irradiated within rectangular fields of $130 \times 130\ \mu m^2$. Ion beam was provided by Jeol JIB 4601F dual beam instrument using the parameters of 30 keV ion energy and ion current in the range of 3 to 60 nA. The beam exposure on as compacted anatase nanoparticles was applied by means of the normal scanning mode (line by line). Corresponding ion doses (ions/cm^2) for each field of irradiation were achieved by varying the total exposure time during the scanning and also ion currents. Ion doses for each region were calculated using the equation:

$$\text{Ion dose (ions/cm}^2) = \frac{Q[C]}{e[C]\times A[cm^2]} = \frac{I[A]\times t[s]}{e[C]\times A[cm^2]}$$

Where $\boldsymbol{Q}$ corresponds to the electron charge and can be calculated from $\boldsymbol{I} \times \boldsymbol{t}$; $\boldsymbol{I}$ is the ion beam current; $\boldsymbol{t}$ is the total exposure time; $\boldsymbol{e}$ (1.602×10^{-19}) is the electron charge; and $\boldsymbol{A}$ is the irradiated area. By using the given equation, it was assumed that the ion dose exposed by means of scanning provided uniform irradiation throughout the selected regions of the sample.

Irradiated anatase samples were then characterized by means of Raman spectroscopy, to build up a correlation between the ion beam irradiation and amorphization, the phase transformations, gallium implantation and production of oxygen vacancies. In addition, an SEM characterization has been carried out on the samples to investigate the morphology evolution of TiO_2 anatase surface during ion beam irradiation.

The SEM analysis was performed on a LYRA 3 FIB/SEM dual beam platform with a field emission electron gun, which is equipped with SE and BSE detectors, in beam SE and BSE detectors and an Oxford EDS detector. Raman measurements were performed on a Raman Renishaw InVia System equipped with 532 nm green laser and 2400 lines/mm grating. A He-Ne laser operating at 633 nm (1.96 eV) was used as excitation source with a laser power of about 3 mW on the sample. The spectra were collected with

an Olympus N-Plan 50×0.75 objective in 30 seconds per spectrum. The great advantage of Raman spectroscopy compared to infrared spectroscopy is its enhanced lateral resolution (around 1 μm).

Table 2 Ion doses calculated upon beam exposure times and currents

I(A)	t(s)	Dose(Ion/cm^2)
3.00E-09	480	5.32E+16
3.00E-09	1845	2.04E+17
1.00E-08	1506	5.56E+17
6.00E-08	5599	1.24E+19

3.4. Surface morphology evolution during ion beam irradiation

Low energy (50 – 1000 eV) ion bombardment is a common technique to produce nano-sized patterns on various materials. It is well known that under certain conditions ion sputtering produces certain patterns on surfaces. TiO_2 anatase as a cheap and chemically stable material has gained interest in energy storage systems. Moreover manipulating the surface morphology is a path to gain higher performance in energy storage materials. Among different morphologies nano-needle shape structure is a desired structure. Focused ion beam irradiation is one way in order to produce various types of nano structures especially nanoneedles. Generally, these typical nano structures formed at the temperature below the melting point of target material. Nanoneedle shape structures were reported so far for tungsten[68] and 18Cr-ODS steel[69]. A cause for the evolution of nanoneedle structure during ion bombardment was proposed as being due to the competition between surface roughening introduced by sputtering and smoothing created by various processes, such as curvature dependent sputtering[70], [71] thermal diffusion[72] redeposition and ion induced diffusion[73], [74] viscous flow[72], [75] and preferential sputtering without actual mass movement[76], [77]. However, it is still controversial what the mechanism of the nanoneedle structure formation is. The target material and different irradiation condition play a significant role on the surface roughening and morphological evolution. The ion beam irradiation condition can be

categorized as ion mass, beam energy and direction. The final surface pattern is a result of interplay between surface roughening/smoothening kinetics and defects near the surface. The morphology and topography of unirradiated as-compacted anatase is shown in Figure 40. Due to the production method of anatase tablet the surface roughness is high to start with. There are some fine scratch lines and some micro sized pits and significant embossments. As we will see, this morphology affected the sputtering during ion bombardment.

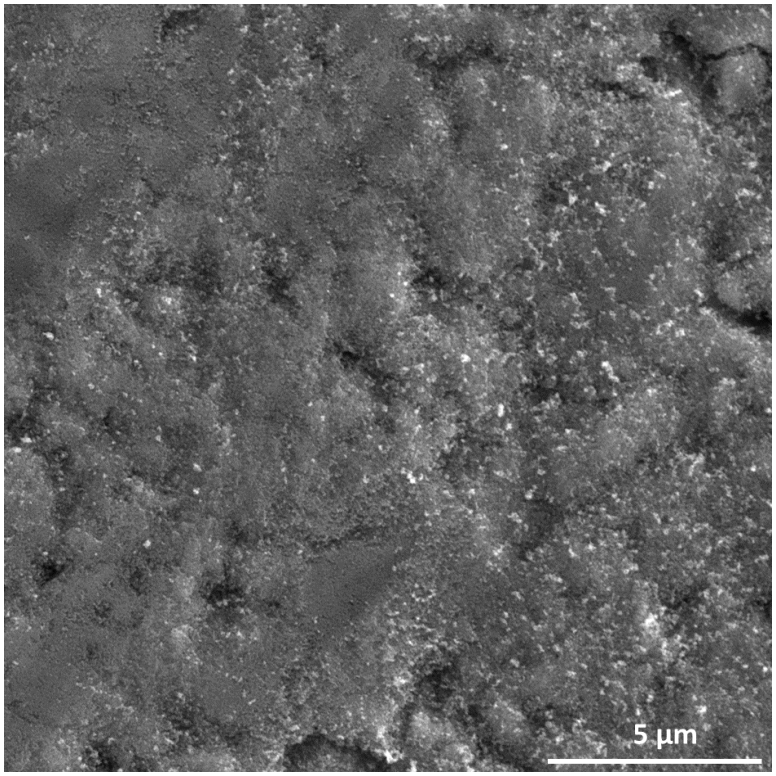

Figure 41 morphology and topography of as-compacted sample

The in-situ SEM/FIB imaging reveals a sequence of evolution of the surface. This evolution can be summarized in 3 distinct stages as shown in Figure 42: 1) the low energy ion sputtering causes further roughening of the anatase surface; 2) small sized pores are produced on the specimen surface and with increasing the ion fluences these pores are enlarged due to coalescence with each other; 3) and finally the formation of nanoneedle-like nano structure. Figure 43 shows nanoneedles with average length of 1 µm and diameter of 50 nm at the tip, formed on anatase surface under 30 keV Ga^+ bombardment at a fluence of 1.24 E19 ion/cm^2 and incident angle of 55º. The direction of nanoneedles are aligned with ion beam direction. With further increasing of ion fluence, the nanoneedles become finer and longer. A similar phenomenon was also observed on pure

tungsten and 18Cr-ODS steel[68], [69]. Morphological evolution induced by ion bombardment strongly depends on the ion beam

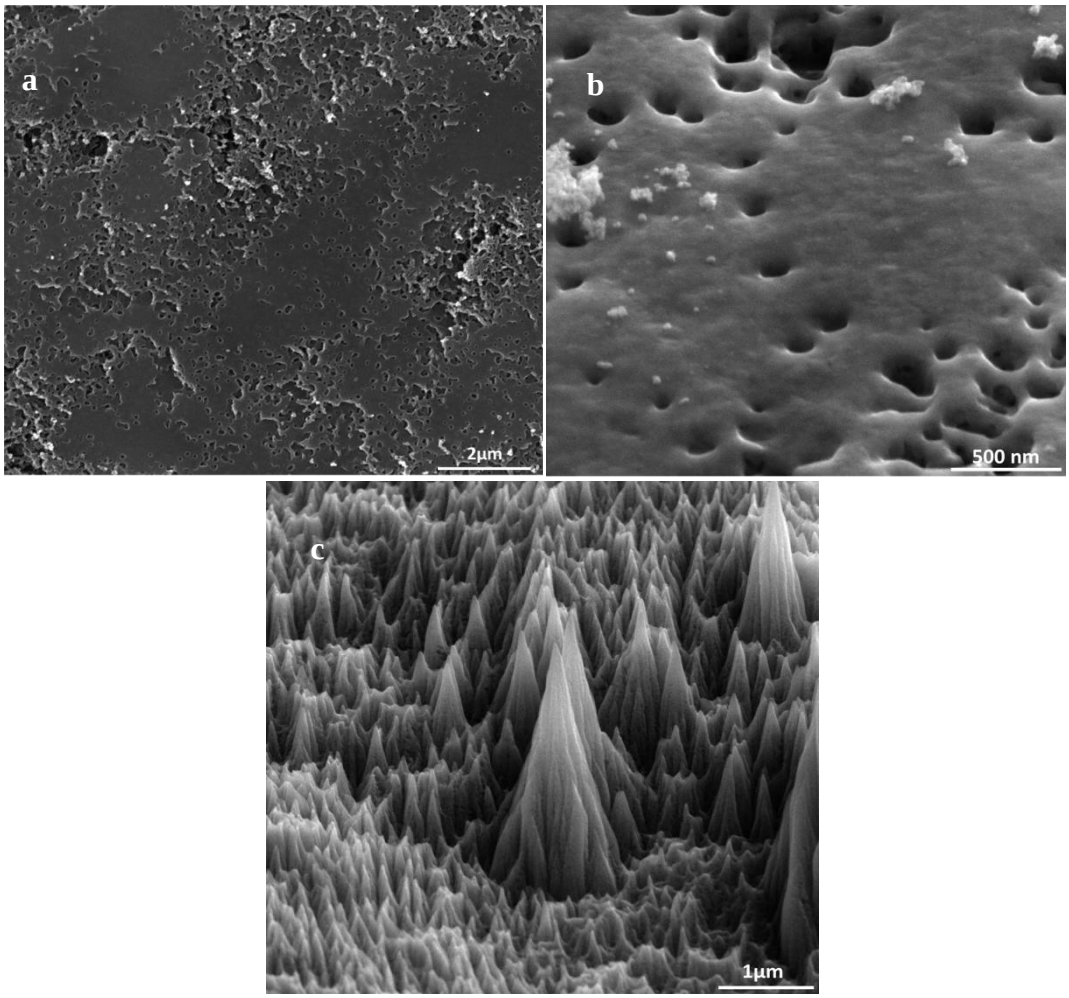

Figure 42 The sequence of morphology evolution and nanoneedle formation during ion beam irradiation a) increasing the raoughness of surface b)

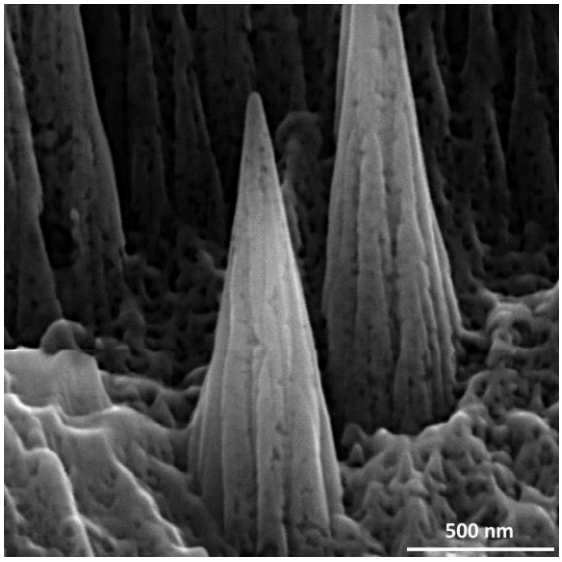

Figure 43 Showing the nanoneedle formed under ion bombardment. The diameter of the nanoneedle at the tip is around 50 nm

conditions (energy, incident angle, etc), and the initial surface morphology as a result of dynamic competition between the surface roughening and smoothing process. The difference between various materials is the different ion fluences threshold for nanoneedle formation at the same bombardment parameters. This can be due to the distinction of material and physical parameters such as heat conduction, surface sputtering ratio. In order to compare the effect of incident beam angle on nanoneedle structure formation the ion beam irradiation with totally same parameters was carried out in different ion beam angles. As shown in figure 44 the effect of ion beam angle with respect to sample surface was investigated. It is obvious that the formation of nano-needles becomes easier with increasing the ion beam angle and the sharpest nano-needles obtained at the irradiation angle of 55º. morphological evolution during ion beam irradiation has been widely investigated during past decades[71]–[77]. One of the most reliable theories has been reported by Bradly and Harper (BH). They suggested a linear instability model to describe the evolution behaviors of surface morphology based on the Sigmund mechanism and surface diffusion.

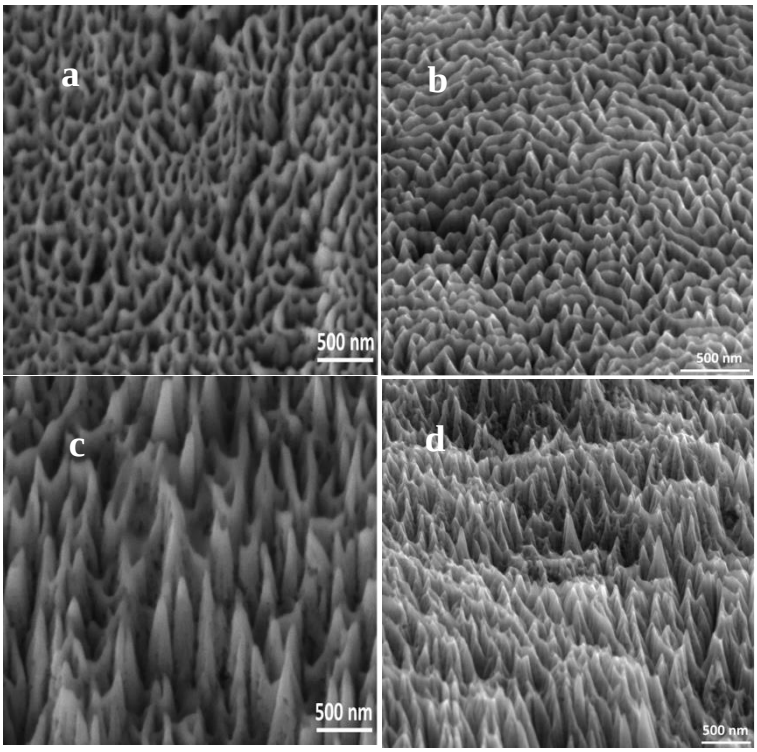

Figure 44 Comparison of formed nanoneedles under two different ion milling angle a) normal to the surface b) 15º tilted c) 35º tilted d) 55º tilted

They claimed that the local sputtering yields were proportional to the surface curvature. It tells that more energy is deposited on a surface with a positive curvature (bottom of valleys) than a surface with a negative curvature (top of hills). Because of this fact, the surface with a positive curvature is eroded faster than that with a negative curvature.

On the other hand Cuerno and Barabasi[76], [77] provided a nonlinear model derived from stochastic differential equations on the basis of Bradley and Harper's second-order linear equation by adding nonlinear and fourth-order terms, which could be used to explain the nanoneedle saturation and fluence dependence of nanoneedle length. The generalized theory introduced an ion-induced smoothing mechanism via preferential sputtering without mass movement on the surface. The sputtering and diffusion kinetics also governed by the surface curvatures which cause localized variation in the incident angle. The nanosized pits and embossments may serve as the original sites for nanoneedle formation. As the ion fluence increases the holes develop in the depth direction. These holes with positive curvature is a preferential sites for sputtering. Over all a surface with different curvatures may cause localized variation in incident angle and this property leads to a change in diffusion kinetics and even roughening in the presence of barriers to interlayer diffusion. The competition of the sputtering-induced sputtering and ion beam-driven surface smoothening results in the eventual formation of the nanoneedles upon focused Ga+ ion bombardment. In addition Guang Ran et al have shown that the initial surface morphology and imperfections have a significant impact on the kinetics of surface roughening and nanoneedle formation[69]. The results of their study proved that the defects near surface enhance the kinetics of surface roughening and nanoneedle formation. Particularly, the existing defects and morphological variation near surfaces significantly affect the dynamic competition of atom loss on the surface due to sputtering, the vacancies gathering, and supply of atoms on the subsurface. As it is shown in Figure 40, the as-compacted sample has some holes on the surface. These holes develop in the depth direction via coalescence of the hole upon subsequent Ga^+ bombardment. The structure will evolve into a nano-needle pattern due to a curvature-dependent sputtering yield. The interplay between surface roughening and defect accumulation determined the final surface patterns.

3.5. Amorphization, gallium implantation and oxygen vacancy production during ion beam irradiation

As previously mentioned amorphization and gallium implantation are two main effects of low energy ion beam irradiation. Amorphization occurs when the incident ion beam energy or dose is not enough to cause sputtering and remove the material. In the current study amorphization occurred during irradiation with low ion beam doses. With increasing the ion dose the surface became smoother and self-assembly patterns started to form. This phenomenon can be understood from the raman spectra of irradiated surface. From the Raman spectra it is obvious that the two main peaks of 399 cm^{-1} ($B_{1g(1)}$) and 540 cm^{-1} (combination of A_{1g} and $B_{1g(2)}$ that cannot be determined at room temperature) are diminished due to amorphization. In addition, low densities of characteristic peaks of Raman spectra are another result of amorphization (Fig. 44). On the other hand, gallium implantation has been observed in sample surface due to high energy of collided ions. This can be observed from the red shift of Eg(3) characteristic peak (Fig. 45). Various determinants may cause the changes in the peak position. Among them we can mention some of the most important factors such as phonon confinement strain, non-homogeneity of the particle size, distribution defects and nonstoichiometry as well as anharmonic effects. The Eg(3) Raman peak shifted to lower wavenumbers as the Ga-doping content increase for both samples prepared by sol-gel method and forced hydrolysis method. The Eg(3) characteristic peak of anatase has shifted 10 wavenumber from 638.7 for as-compacted sample to 628.7 for irradiated sample with 1.24 E19 ion fluence as shown in Figure 46.

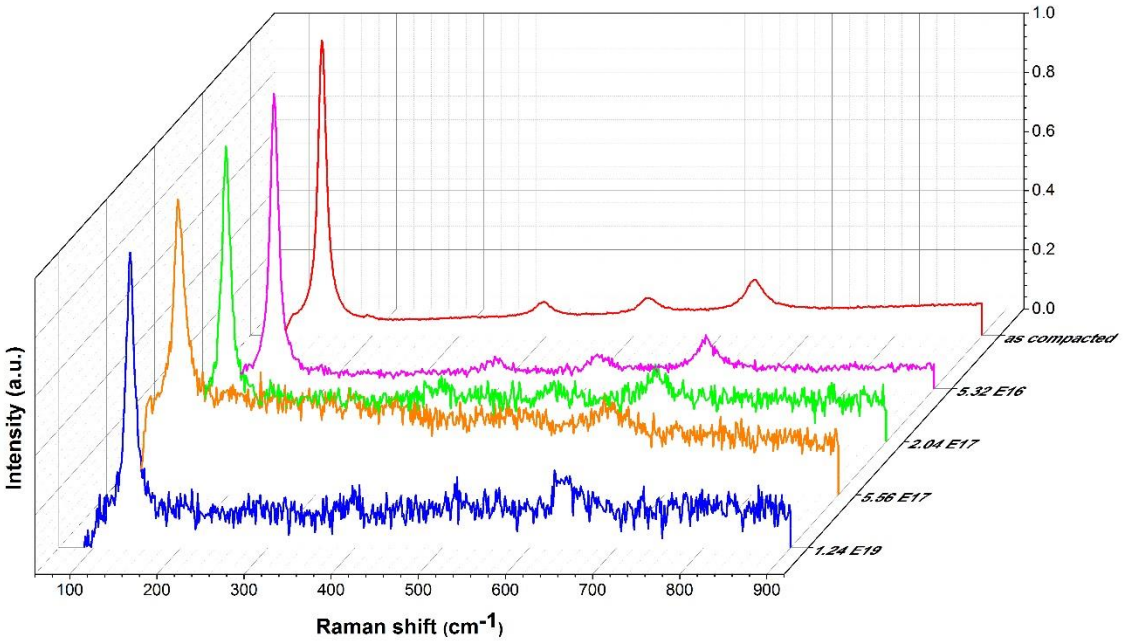

Figure 45 Raman spectra of as-compacted and irradiated samples

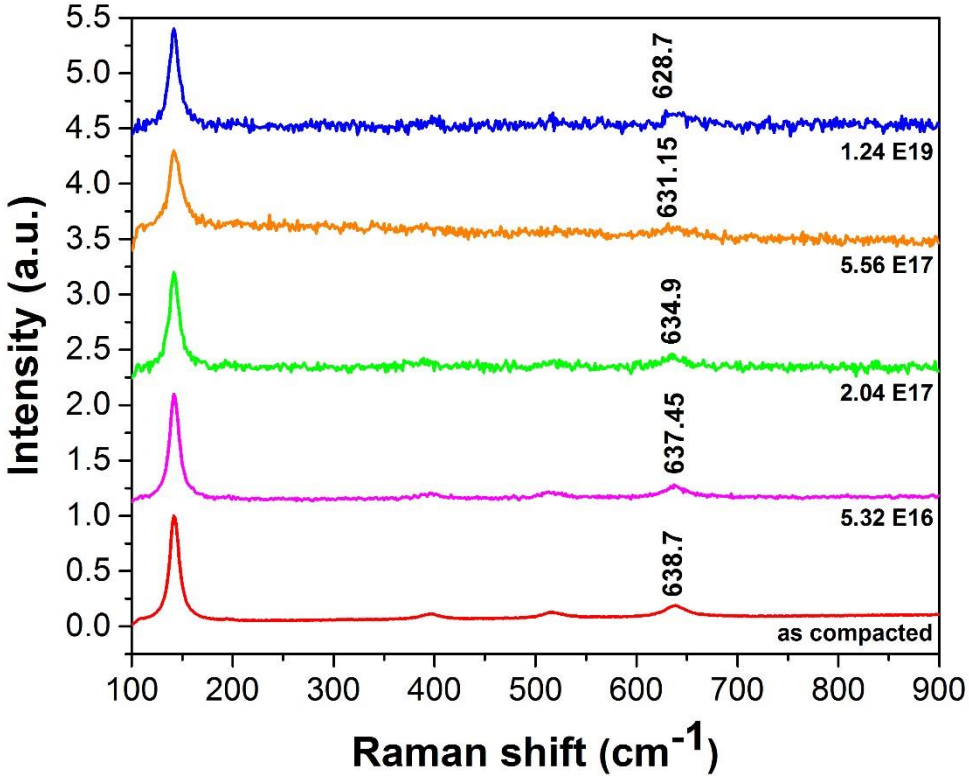

Figure 46 Red shift in Eg(3) characteristic peak due to ion implantation

The EDS analysis of irradiated surface is another proof for the phenomenon of gallium implantation as shown in Figure 47. The amount of gallium implanted in anatase surface reached to a value of 10% for ion fluence of 1.24 E19 ion/cm^2.

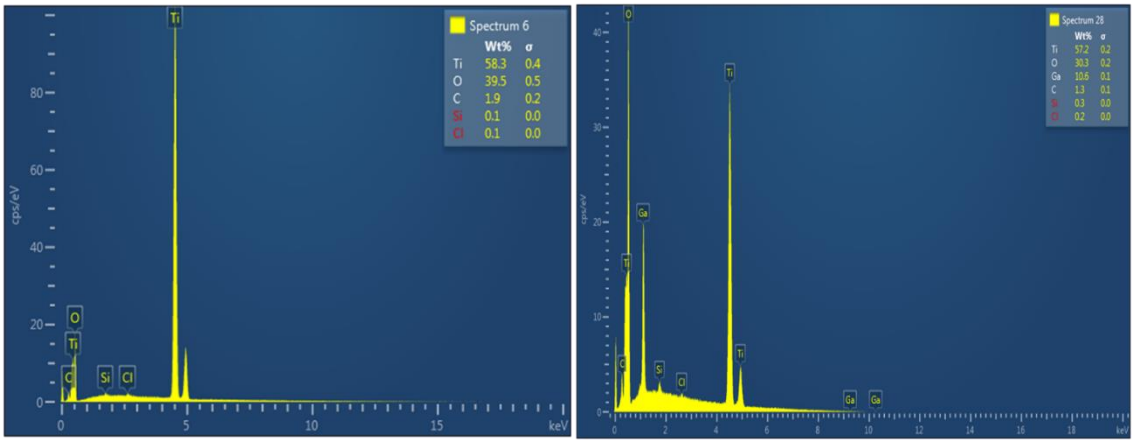

Figure 47 EDS analysis of as-compacted and irradiated anatase

In order to gain insight into the implantation and distribution of Ga^+ ions on the surface of TiO_2, the depth distribution of implanted Ga+ ions and the collision cascade the Stopping and Range of Ions in Matter (SRIM) 2008 has been used for the plantations which were simulated by detailed Monte Carlo calculations. This software package called SRIM (Stoping and Range of Ions in Matters) / TRIM (Transport of Ions in Matter) has a wide variety of usage for predicting sputter yields for many various ions at a wide energy range. The SRIM/TRIM software typically uses a Monte Carlo simulation of ion-atom collisions to calculate the stopping range of ions into the matter. Also the experimental data matches very well with SRIM/TRIM calculation. According to this simulation besides material itself, various parameters such as ion energy, angle of incidence and scanning procedures affect the sputter yield[27]. Figure 48 and 49 shows the TRIM simulation for Ga^+ ion penetration depth and the collision cascade for ions with 30 keV energy in two different angles of 0º and 55º. It can be deduced from the images that the maximum penetration depth of gallium ion into the TiO_2 surface is around 70 nm in 0º ion incident direction but the collision cascade for this energy and angle of gallium ion beam is even more around 100 nm. However, with tilting the beam to the angle of 55º it can be seen that the ion implantation limited to around 50 nm and the collision cascade decreases to about 80 nm.

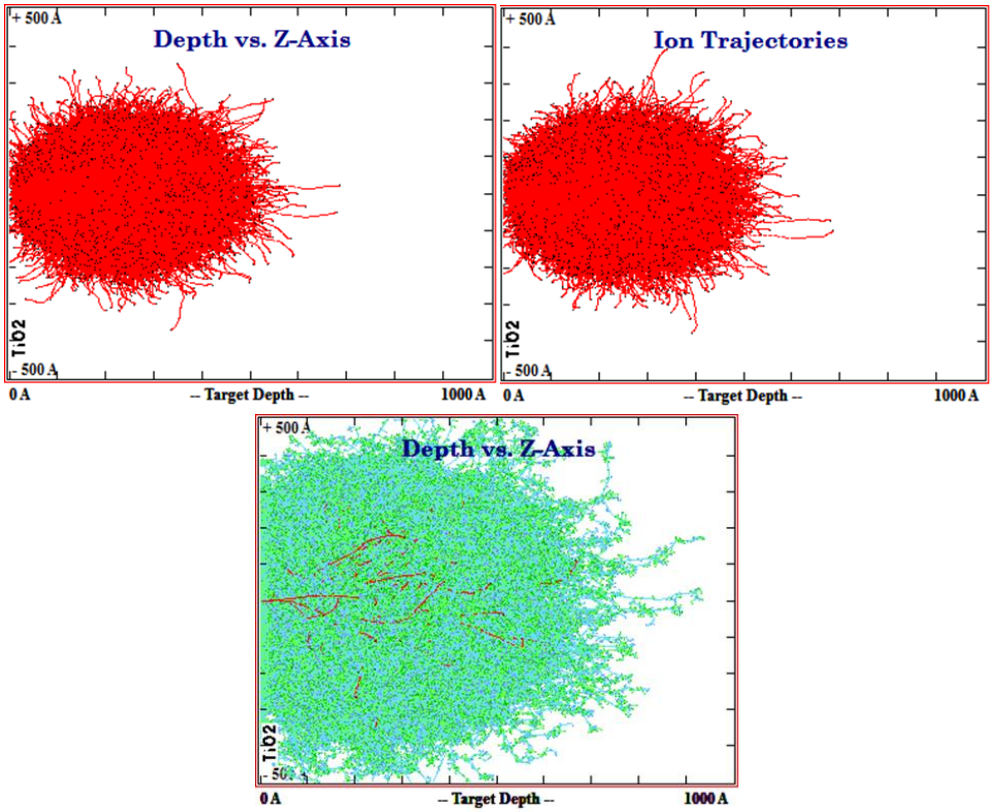

Figure 48 TRIM simulation of Ga^+ ion penetration into TiO_2 surface in zero tilt

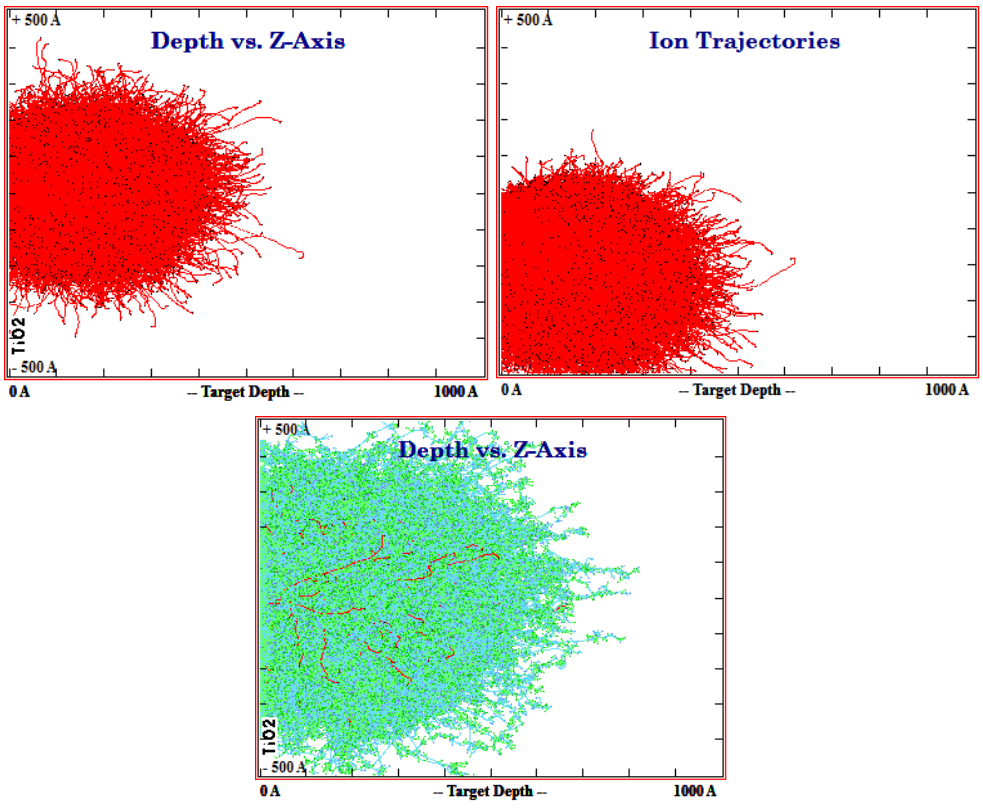

Figure 49 TRIM simulation of Ga^+ ion penetration into TiO_2 surface in 55° tilt

The other side effect of ion bombardment during surface irradiation by focused ion beam is introducing defects such as oxygen vacancies on the material. This phenomenon can be interpreted with the fact that during production of oxygen vacancy the main characteristic Raman peak ($E_{g(1)}$) of anatase becomes broader as shown in Figure 51. Here the FWHM (Full width at half maximum) for as compacted sample is 11.2, this value for the sample, which irradiated with ion fluence of 1.24 E19 ion/cm^2 is around 13.5.

As a consequence with image analysis of acquired SEM image by ImageJ software the following conclusion can be drawn. With increasing the ion dose the amorphization starts to take place on the surface of the anatase TiO_2, with continuing the ion beam irradiation small sized pores are produced on the surface and after a minor increasing of ion beam dose these pores starts to enlarge due to coalescence with each other. This procedure goes on with oxygen vacancy production and finally stabilized in a certain nanostructure, which will be explained in subsequent section. Figure 50 shows a graph of ion dose versus material removal during ion beam irradiation. This graph shows different aforementioned steps in detail.

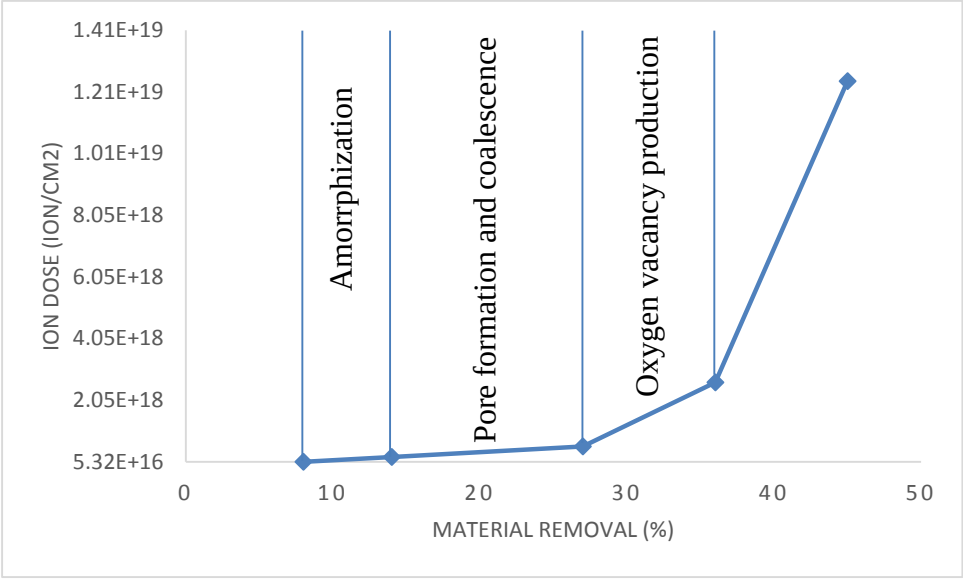

Figure 50 SEM image analysis showing the material removal versus ion dose and different phenomena occured during ion beam irradiation of anatase surface

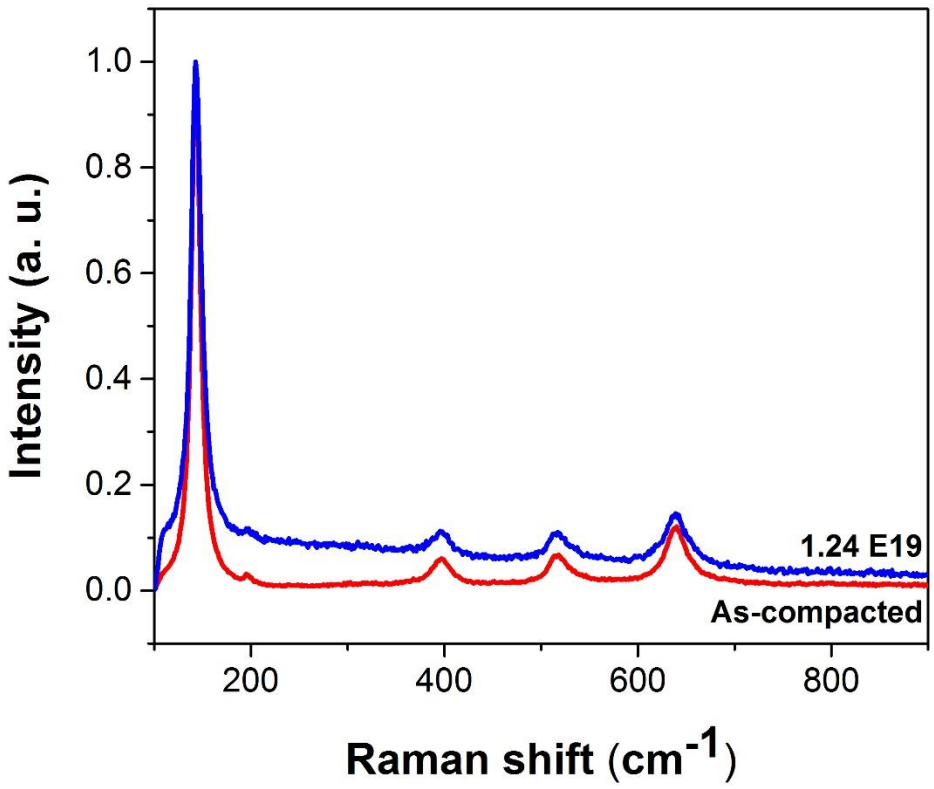

Figure 51 Peak broadening of main characteristic peak of anatase due to oxygen vacany

3.6. Gas assisted etching of anatase surface

The fundamental of gas assisted FIB induced etching relies on the process including removal of a volatile compound by system vacuum, which is produced by reacting a gas and the sample surface. The steps in the gas assisted focused ion beam etching process are as follows:

(1) A chemically neutral reactive gas is introduced through a fine gas nozzle and is adsorbed (or chemisorbed) on the sample surface.

(2) The gas reacts with the sample either spontaneously, as in silicon and fluorine, or in the presence of the ion beam the gas decomposes and reacts with the sample, as with water and carbon based polymers.

(3) The volatile products leave the surface (desorption).

In the current study a XeF_2 assisted etching was performed on the anatase surface with ion fluence of 1.24 E19 ion/cm^2. The surface morphology became smoother as shown in Figure 52.

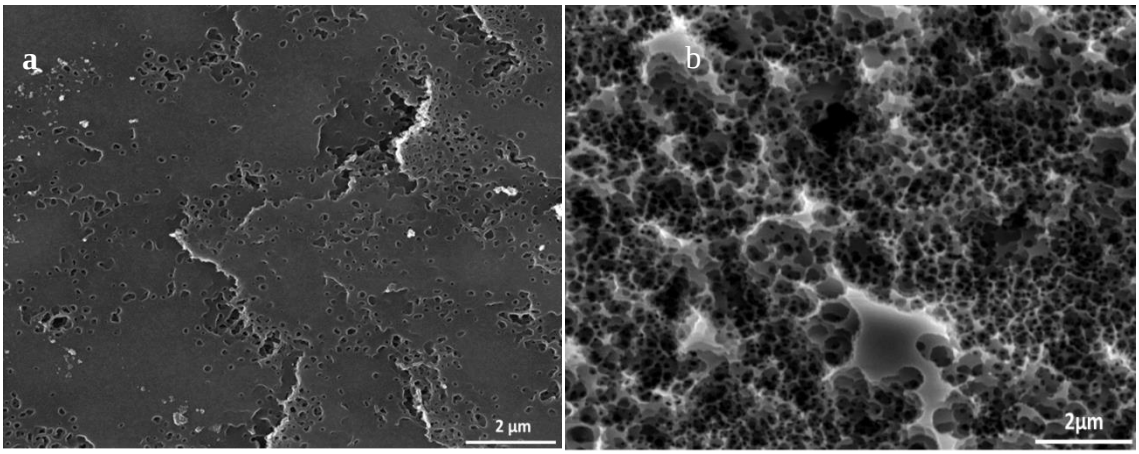

Figure 52 Comparison of surface roughness and amorphization between a) direct milling b) gas assisted etching

The gallium implantation decreases due to presence of fluorine. The Raman spectra of as-compacted sample and irradiated sample in the presence of XeF_2 shows almost the same characteristic peaks and no drastic shift or peak broadening was observed (Fig. 53). The EDS mapping investigation shows that the fluorine oxide (F_2O) phase was produced during ion irradiation (Fig. 54).

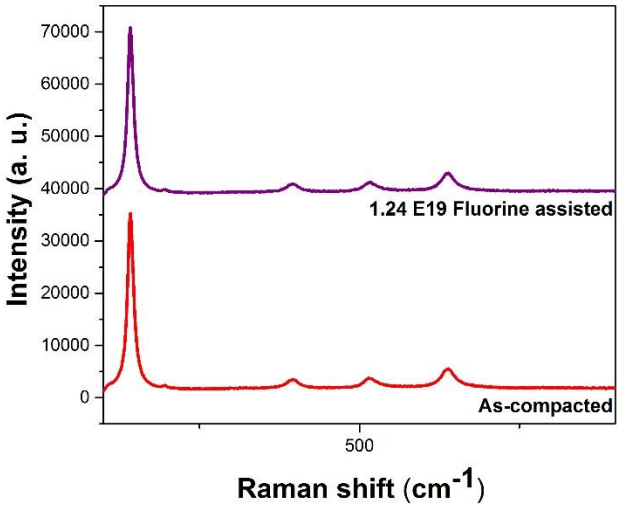

Figure 53 Raman spectra of as-compacted and gas assisted etched anatase surface

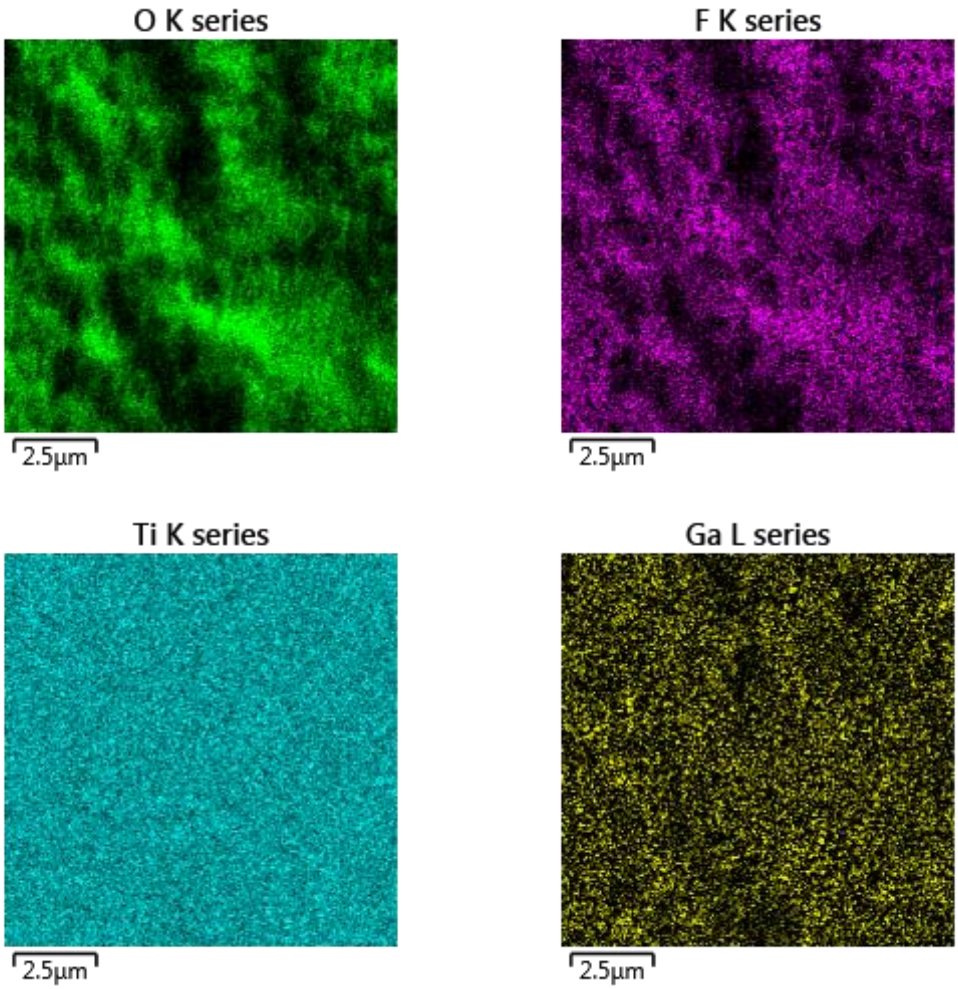

Figure 54 EDS mapping of irradiated TiO_2 surface in presence of XeF_2

4. Conclusion

In this work, complimentary electron microscopy analysis including Focused Ion Beam (FIB), Scanning Electron Microscopy (SEM) and high resolution Transmission Electron Microscopy (TEM) were used for observing micro and nanodetails within human dentin. Dual-beam instruments allowed for preparing pin-like uniform and representative 3D TEM specimens using ion-milling and deposition based advanced nanostructuring techniques. This was followed by acquiring related secondary electron (SE) image tomographs of stacking the images from FIB slice-series for monitoring micro-sized dentinal tubules. FIB-structured pin-like samples were investigated at the TEM for observing the nanometer sized collagen fibrils that form dentinal tissues. Consequently, this study enabled for revealing the microstructure and morphology of human dentin in three dimensions for both its micro and nano constituents.

The low energy ion irradiation was carried on on anatse TiO_2 surface by focused Ga^+ ion bombardment for the reason of exploring the surface morphology and surface transformation of this material. A polycrystalline nanoneedle structure forms without chemical composition change. The formation of nanoneedle is a result of a curvature-dependent sputtering yield while the surface is bombarded by ion beam. affecting the dynamic competition of atom loss on the surface, the vacancies gathering, and atom supply from the subsurface. The nanoneedle formation was enhanced with increasing the ion beam direction angle. The surface roughness plays a crucial role in anatase nanoneedle formation while the surface is bombarded by ion beam. This method of creating anatase TiO_2 nanoneedle is a potential method to produce a nanostructure which is desirable in a wide range of applications especially energy storage and electrical materials such as batteries and diodes and biomaterials specifically in dentistry.

5. References

[1] W. Zhou, R. P. Apkarian, and Z. L. Wang, “Fundamentals of Scanning Electron Microscopy,” *Scanning Microsc. Nanotechnol.*, pp. 1–40, 2007.

[2] L. Reimer, *Scanning electron microscopy*. springer, 1998.

[3] O. Wells, A. Boyde, E. Liftshin, and A. Rezanowich, *Scanning Electron Microscopy*. McGraw Hill, 1974.

[4] C. Volkert and A. Minor, “Focused Ion Beam microscopy and micromachanning,” *MRS Bull.*, vol. 32, pp. 389–395, 2007.

[5] L. A. Giannuzzi and F. A. Stevie, “Introduction to focused ion beams: Instrumentation, theory, techniques and practice,” *Introd. to Focus. Ion Beams Instrumentation, Theory, Tech. Pract.*, pp. 1–357, 2005.

[6] J. Orloff, M. Utlaut, and L. Swanson, *High Resolution Focused Ion Beams*. Kluwer Academic/Plenum Publishers, New York, 2002.

[7] “United States Patent,” 4315153.

[8] N. Silvis-Cividjian, C. W. Hagen, L. H. A. Leunissen, and P. Kruit, “The role of secondary electrons in electron-beam-induced-deposition spatial resolution,” *Microelectron. Eng.*, vol. 61–62, pp. 693–699, 2002.

[9] M. Schaffer and J. Wagner, “Block lift-out sample preparation for 3D experiments in a dual beam focused ion beam microscope,” *Microchim. Acta*, vol. 161, no. 3–4, pp. 421–425, 2008.

[10] J. Mayer, L. A. Giannuzzi, T. Kamino, and J. Michael, “TEM Sample Preparation and FIB-Induced Damage,” *MRS Bull.*, vol. 32, no. 05, pp. 400–407, 2007.

[11] R. M. Langford and C. Clinton, “In situ lift-out using a FIB-SEM system,” *Micron*, vol. 35, pp. 607–611, 2004.

[12] R. E. Dunin-Borkowski, S. B. Newcomb, T. Kasama, M. R. McCartney, M. Weyland, and P. a. Midgley, “Conventional and back-side focused ion beam milling for off-axis electron holography of electrostatic potentials in transistors,” *Ultramicroscopy*, vol. 103, no. 1, pp. 67–81, 2005.

[13] J. Li, T. Malis, and S. Dionne, “Recent advances in FIB–TEM specimen preparation techniques,” *Mater. Charact.*, vol. 57, no. 1, pp. 64–70, 2006.

[14] R. M. Langford and A. K. Petford-Long, “Preparation of transmission electron microscopy cross-section specimens using focused ion beam milling,” *J. Vac. Sci. Technol. A Vacuum, Surfaces, Film.*, vol. 19, no. 5, p. 2186, 2001.

[15] G. S. Park, “Cross-sectional TEM studies of transparent thin multilayers on polymeric substrates utilizing ultramicrotomy,” *Surf. Coat. Technol.*, vol. 115, no. 1, pp. 52–56, 1999.

[16] B. Van Leer and L. Giannuzzi, “Static vs. Dynamic FIB/SEM Methods For 3D Modeling,” *Microsc. Microanal.*, vol. 13, no. S02, pp. 1506–1507, 2007.

[17] A. Volinsky, “FIB failure analysis of memory arrays,” *Microelectron. Eng.*, vol. 75, no. 1, pp. 3–11, 2004.

[18] M. D. Uchic, L. Holzer, B. J. Inkson, E. L. Principe, and P. Munroe, “Three-Dimensional Microstructural Characterization Using Focused Ion Beam Tomography,” *MRS Bull.*, vol. 32, no. 05, pp. 408–416, 2007.

[19] L. Holzer, F. Indutnyi, P. Gasser, B. Münch, and M. Wegmann, “Three-dimensional analysis of porous BaTiO3 ceramics using FIB nanotomography,” *J. Microsc.*, vol. 216, no. April, pp. 84–95, 2004.

[20] N. Vivet, S. Chupin, E. Estrade, T. Piquero, P. L. Pommier, D. Rochais, and E. Bruneton, “3D Microstructural characterization of a solid oxide fuel cell anode reconstructed by focused ion beam tomography,” *J. Power Sources*, vol. 196, no. 18, pp. 7541–7549, 2011.

[21] D. Kiener, C. Motz, M. Rester, M. Jenko, and G. Dehm, “FIB damage of Cu and possible consequences for miniaturized mechanical tests,” *Mater. Sci. Eng. A*, vol. 459, pp. 262–272, 2007.

[22] M. D. Uchic, D. M. Dimiduk, J. N. Florando, and W. D. Nix, “Sample dimensions influence strength and crystal plasticity.,” *Science*, vol. 305, no. 5686, pp. 986–9, 2004.

[23] R. D. Field and P. A. Papin, “Location specific in situ TEM straining specimens made using FIB,” *Ultramicroscopy*, vol. 102, no. 1, pp. 23–26, 2004.

[24] J. R. Greer, W. C. Oliver, and W. D. Nix, “Size dependence of mechanical properties of gold at the micron scale in the absence of strain gradients,” *Acta*

Mater., vol. 53, no. 6, pp. 1821–1830, 2005.

[25] R. F. Egerton, P. Li, and M. Malac, "Radiation damage in the TEM and SEM," *Micron*, vol. 35, no. 6, pp. 399–409, 2004.

[26] T. J. Shaffner and R. D. Van Veld, "'Charging' effects in the scanning electron microscope," *J. Phys. E.*, vol. 4, pp. 633–637, 1971.

[27] A. A. Tseng, "Recent Developments in Nanofabrication Using Focused Ion Beams," *Small*, vol. 1, no. 10, pp. 924–939, 2005.

[28] B. Basnar, A. Lugstein, H. Wanzenboeck, H. Langfischer, E. Bertagnolli, and E. Gornik, "Focused ion beam induced surface amorphization and sputter processes," *J. Vac. Sci. Technol. B Microelectron. Nanom. Struct.*, vol. 21, no. 3, p. 927, 2003.

[29] C. A. Volkert, A. M. Minor, G. Editors, and B. May, "Focused Ion Beam Micromachining," vol. 32, no. May, pp. 389–399, 2007.

[30] J. J. L. Mulders, D. a M. de Winter, and W. J. H. C. P. Duinkerken, "Measurements and calculations of FIB milling yield of bulk metals," *Microelectron. Eng.*, vol. 84, no. 5–8, pp. 1540–1543, 2007.

[31] C. A. Volkert and A. M. Minor, "Focused Ion Beam Microscopy and Micromachining," *MRS Bull.*, vol. 32, no. 05, pp. 389–399, 2007.

[32] F. A. Stevie, L. A. Giannuzzi, and B. I. Prenitzer, "The Focused Ion Beam Instrument," in *Introduction to Focused Ion Beams*, Boston: Kluwer Academic Publishers, pp. 1–12.

[33] J. P. McCaffrey, M. W. Phaneuf, and L. D. Madsen, "Surface damage formation during ion-beam thinning of samples for transmission electron microscopy," *Ultramicroscopy*, vol. 87, no. 3, pp. 97–104, 2001.

[34] J. Mayer, L. a Giannuzzi, T. Kamino, and J. Michael, "T EM Sample Preparation and Damage," *MRS Bull.*, vol. 32, no. 5, pp. 400–407, 2007.

[35] W. J. MoberlyChan, D. P. Adams, M. J. Aziz, G. Hobler, and T. Schenkel, "Fundamentals of Focused Ion Beam Nanostructural Processing: Below, At, and Above the Surface," *MRS Bull.*, vol. 32, no. 05, pp. 424–432, 2007.

[36] A. M. Datesman, J. C. Schultz, T. W. Cecil, C. M. Lyons, and A. W. Lichtenberger, "Gallium ion implantation into niobium thin films using a focused-ion beam,"

IEEE Trans. Appl. Supercond., vol. 15, no. 2 PART III, pp. 3524–3527, 2005.

[37] H. D. Wanzenboeck, H. Langfischer, A. Lugstein, E. Bertagnolli, U. Grabner, P. Pongratz, B. Basnar, J. Smoliner, and E. Gornik, "Effects of Ga-Irradiation On Properties of Materials Processed by A Focused Ion Beam (FIB)," *MRS Proc.*, vol. 647, p. O6.6, Jan. 2000.

[38] L. Frey, C. Lehrer, and H. Ryssel, "Nanoscale effects in focused ion beam processing," *Appl. Phys. A Mater. Sci. Process.*, vol. 76, no. 7, pp. 1017–1023, 2003.

[39] W. Y. Kwong and W. Y. Zhang, "Electron-beam assisted platinum deposition as a protective layer for FIB and TEM applications," *ISSM 2005, IEEE Int. Symp. Semicond. Manuf. 2005.*, pp. 469–471, 2005.

[40] R. Jamison, A. Mardinly, D. Susnitzky, and R. Gronsky, "Effects of ion species and energy on the amorphization of Si during FIB TEM sample preparation as determined by computational and experimental methods," *Microsc. Microanal. YORK*, vol. 6, no. 2, pp. 526–527, 2000.

[41] A. Rota, S. F. Contri, G. C. Gazzadi, S. Cottafava, E. Gualtieri, and S. Valeri, "Focused ion beam induced swelling in MgO(001)," *Surf. Sci.*, vol. 600, no. 18, pp. 3718–3722, 2006.

[42] D. D. Arola and R. K. Reprogel, "Tubule orientation and the fatigue strength of human dentin," *Biomaterials*, vol. 27, no. 9, pp. 2131–2140, 2006.

[43] M. Sezen and S. Sadighikia, "3D electron microscopy investigations of human dentin at the micro/nano-scale using focused ion beam based nanostructuring," *RSC Adv.*, vol. 5, pp. 7196–7199, 2015.

[44] M. H. Ross, G. I. Kaye, and W. Pawlina, *Histology: a text and atlas: with cell and molecular biology*. Lippincott Williams \& Wilkins, 2003.

[45] S. Habelitz, M. Balooch, S. J. Marshall, G. Balooch, and G. W. M. Jr, "In situ atomic force microscopy of partially demineralized\rhuman dentin collagen fibrils," *J. Struct. Biol.*, vol. 138, pp. 227–236, 2002.

[46] D. S. Brauer, J. F. Hilton, G. W. Marshall, and S. J. Marshall, "Nano- and micromechanical properties of dentine: Investigation of differences with tooth side," *J. Biomech.*, vol. 44, no. 8, pp. 1626–1629, 2011.

[47] M. B. Lopes, M. a C. Sinhoreti, A. Gonini Júnior, S. Consani, and J. F. McCabe,

"Comparative study of tubular diameter and quantity for human and bovine dentin at different depths," *Braz. Dent. J.*, vol. 20, no. 4, pp. 279–283, 2009.

[48] T. Teeth and T. Environment, *The Teeth and their oral environment*. 2005.

[49] P. T. Pires, J. C. Ferreira, S. a Oliveira, A. F. Azevedo, W. R. Dias, and P. R. Melo, "Shear bond strength and SEM morphology evaluation of different dental adhesives to enamel prepared with ER:YAG laser.," *Contemp. Clin. Dent.*, vol. 4, no. 1, pp. 20–6, 2013.

[50] G. Pfaff and P. Reynders, "Angle-Dependent Optical Effects Deriving from Submicron Structures of Films and Pigments," *Chem. Rev. (Washington, D. C.)*, vol. 99, no. 7, pp. 1963–1981, 1999.

[51] S. Yuan, W. Chen, and S. Hu, "Fabrication of TiO2 nanoparticles/surfactant polymer complex film on glassy carbon electrode and its application to sensing trace dopamine," *Mater. Sci. Eng. C*, vol. 25, no. 4, pp. 479–485, 2005.

[52] J. H. Braun, A. Baidins, and R. E. Marganski, "TiO2 pigment technology: a review," *Prog. Org. Coatings*, vol. 20, no. 2, pp. 105–138, May 1992.

[53] A. Salvador, M. C. Pascual-Martí, J. R. Adell, A. Requeni, and J. G. March, "Analytical methodologies for atomic spectrometric determination of metallic oxides in UV sunscreen creams," *J. Pharm. Biomed. Anal.*, vol. 22, pp. 301–306, 2000.

[54] R. Zallen and M. P. Moret, "The optical absorption edge of brookite TiO2," *Solid State Commun.*, vol. 137, no. 3, pp. 154–157, 2006.

[55] A. Fujishima and K. Honda, "Photolysis-decomposition of water at the surface of an irradiated semiconductor," *Nature*, vol. 238, no. 5385, pp. 37–38, 1972.

[56] A. Fujishima, T. N. Rao, and D. A. Tryk, "Titanium dioxide photocatalysis," *J. Photochem. Photobiol. C Photochem. Rev.*, vol. 1, no. 1, pp. 1–21, 2000.

[57] D. A. Tryk, A. Fujishima, and K. Honda, "Recent topics in photoelectrochemistry: achievements and future prospects," *Electrochim. Acta*, vol. 45, no. 15–16, pp. 2363–2376, 2000.

[58] X. Chen and S. S. Mao, "Titanium dioxide nanomaterials: Synthesis, properties, modifications and applications," *Chem. Rev.*, vol. 107, no. 7, pp. 2891–2959, 2007.

[59] X. Chen, Y. Lou, S. Dayal, X. Qiu, R. Krolicki, C. Burda, C. Zhao, and J. Becker, "Doped Semiconductor Nanomaterials," *J. Nanosci. Nanotechnol.*, vol. 5, no. 9, pp. 1408–1420, Sep. 2005.

[60] Z. F. Yin, L. Wu, H. G. Yang, and Y. H. Su, "Recent progress in biomedical applications of titanium dioxide.," *Phys. Chem. Chem. Phys.*, vol. 15, no. 14, pp. 4844–58, 2013.

[61] A. Labouriau and W. L. Earl, "Titanium solid-state NMR in anatase, brookite and rutile," *Chem. Phys. Lett.*, vol. 270, no. 3–4, pp. 278–284, 1997.

[62] T. Ohsaka, F. Izumi, and Y. Fujiki, "Raman Spectrum of Anatase, TiO," *J. RAMAN Spectrosc.*, vol. 7, no. 6, pp. 321–324, 1978.

[63] "Introduction to Raman Spectroscopy." [Online]. Available: http://bwtek.com/raman-introduction-to-raman-spectroscopy/.

[64] D. B. Williams and C. B. Carter, *Transmission Electron Microscopy*. 1996.

[65] T. Uusimäki, G. Margaris, K. Trohidou, P. Granitzer, K. Rumpf, M. Sezen, and G. Kothleitner, "Three dimensional quantitative characterization of magnetite nanoparticles embedded in mesoporous silicon: local curvature, demagnetizing factors and magnetic Monte Carlo simulations.," *Nanoscale*, vol. 5, no. 23, pp. 11944–53, 2013.

[66] J. Voegel and R. Frank, "Ultrastructural study of apatite crystal dissolution in human dentine and bone," *J. Biol. Buccale*, vol. 5, no. 3, pp. 181–194, 1977.

[67] V. Ziv and S. Weiner, "Bone Crystal Sizes: A Comparison of Transmission Electron Microscopic and X-Ray Diffraction Line Width Broadening Techniques," *Connect. Tissue Res.*, vol. 30, no. 3, pp. 165–175, Jan. 1994.

[68] G. Ran, X. Liu, J. Wu, X. Zu, and L. Wang, "The effect of surface roughness on self-assembly tungsten nanoneedles induced by focused Ga+ ion beam bombardment," *Appl. Surf. Sci.*, vol. 258, no. 15, pp. 5553–5557, 2012.

[69] G. Ran, N. Chen, R. Qiang, L. Wang, N. Li, and J. Lian, "Surface morphological evolution and nanoneedle formation of 18Cr-ODS steel by focused ion beam bombardment," *Nucl. Instruments Methods Phys. Res. Sect. B Beam Interact. with Mater. Atoms*, vol. 356–357, pp. 103–107, 2015.

[70] R. Cuerno and A.-L. Barabasi, "Dynamic scaling of ion-sputtered surfaces," *Phys. Rev. Lett.*, vol. 74, no. 23, pp. 4746–4749, 1995.

[71] R. M. Bradley, “Theory of ripple topography induced by ion bombardment,” *J. Vac. Sci. Technol. A Vacuum, Surfaces, Film.*, vol. 6, no. 4, p. 2390, Jul. 1988.

[72] W. W. Mullins, “Theory of Thermal Grooving,” *J. Appl. Phys.*, vol. 28, no. 3, p. 333, 1957.

[73] M. Castro, R. Cuerno, L. Vázquez, and R. Gago, “Self-organized ordering of nanostructures produced by ion-beam sputtering,” *Phys. Rev. Lett.*, vol. 94, no. 1, pp. 1–4, 2005.

[74] J. Erlebacher, M. J. Aziz, E. Chason, M. B. Sinclair, and J. A. Floro, “Spontaneous pattern formation on ion bombarded Si(001),” *Phys. Rev. Lett.*, vol. 82, no. 11, pp. 2330–2333, 1999.

[75] E. Chason, T. Mayer, B. Kellerman, D. McIlroy, and A. Howard, “Roughening instability and evolution of the Ge(001) surface during ion sputtering,” *Phys. Rev. Lett.*, vol. 72, no. 19, pp. 3040–3043, 1994.

[76] M. A. Makeev and A.-L. Barabási, “Ion-induced effective surface diffusion in ion sputtering,” *Appl. Phys. Lett.*, vol. 71, no. 19, p. 2800, 1997.

[77] S. Park, B. Kahng, H. Jeong, and A.-L. Barabási, “Dynamics of Ripple Formation in Sputter Erosion: Nonlinear Phenomena,” *Phys. Rev. Lett.*, vol. 83, no. 17, pp. 3486–3489, 1999.

List of publications

Refereed Journal Publication

1. **S. Sadighikia**, S. Abdolhosseinzadeh, H. Asgharzadeh, "Production of high porosity Zn foams by powder metallurgy method", *Powder metallurgy. 2015, 58(1), 61-66*

2. M. Sezen, **S. Sadighikia**, "3D electron microscopy investigation of human dentin at the micro/nano-scale using focused ion beam based nanostructuring", *RSC Advances. 2015, 5, 7196-7199*

3. A. Karimzad Ghavidel, T. Azdast, M.R. Shabgard, A. Navidfar, **S. Sadighikia**, "Improving electrical conductivity of poly methyl methacrylate by utilization of carbon nanotube and CO_2 laser", *Journal of Applied Polymer Science, http://onlinelibrary.wiley.com/doi/10.1002/app.42671/full*

4. S. Ghobadi, **S. Sadighikia**, M. Papila, F. Cebeci, S. Alkan Gürsel, "Graphene-reinforced Poly(vinyl alcohol) Electrospun Fibers as Building Blocks for High Performance Nanocomposites", *RSC Advances, 2015,**5**, 85009-85018*

5. S. Abdolhosseinzadeh, H. Asgharzadeh, **S. Sadighikia**, A. Khataee, "UV-assisted synthesis of reduced graphene oxide-ZnO nanorod composites immobilized on Zn foil with enhanced photocatalytic performance" , *Research on Chemical Intermediates, DOI 10.1007/s11164-015-2291-z*

6. S. Abdolhosseinzadeh, **S. Sadighikia**, H. Asgharzadeh, "Scalable synthesis of hydrogenated graphene" *Submitted*

7. M. S. Oskooie, **S. Sadighikia**, H. Asgharzadeh, S. Abdolhosseinzadeh, A. moosavi, M. Salehi, "Corrosion behavior of an Al-Mg-Si alloy with a bimodal grain size distribution". *Submitted*

8. A. Navidfar , T. Azdast, M.R. Shabgard, A. Karimzad Ghavidel, **S. Sadighikia**, S. Mamaghani shishavan, "Influence of CO_2 laser on surface properties of injection molded multi-walled carbon nanotube/poly methyl methacrylate nanocomposite",, *Submitted*

9. A. Karimzad Ghavidel, T. Azdast, M.R. Shabgard, A. Navidfar, **S. Sadighikia**, S. Mamaghani shishavan, "Experimental study of CO_2 laser cutting of anisotropic multi-walled carbon nanotube/poly methyl methacrylate nanocomposites", *Submitted*

Refereed Conference Papers and Abstracts

1. **S. Sadighikia**, M. Sezen, "3D Nanostructuring and Nanoanalysis of Human Enamel and Dentin Using Focused Ion Beams", Oral presentation, *TechConnect World Innovation Conference,Washington, DC, U.S.A, (June 2015)*

2. A.Navidfar, T.Azdast, A.Karimzad Ghavidel, **S.Sadighikia**, S. Mamaghani Shishevan, "Investigation of Rockwell hardness and Charpy impact test of injection molded multi-walled carbon nanotubes/poly methyl methacrylate nanocomposites", Poster session, *5th International Congress on Nanoscience & Nanotechnology (ICNN2014), 22-24 October 2014, Tehran, Iran.*

3. A. Karimzad Ghavidel, T. Azdast, M. Shabgard, A.Navidfar, **S.Sadighikia**, S. Mamaghani Shishevan, "Influence of carbon nanotubes on CO_2 laser cutting workability of multi-walled carbon nanotubes/poly methacrylate nanocomposites", *5th International Congress on Nanoscience & Nanotechnology (ICNN2014), 22-24 October 2014, Tehran, Iran.*